Formation of microfibers and nanofibers by capillary-driven thinning of drying viscoelastic filaments

Jérôme Crest*,[a], Jean-Christophe Nave[b], Santosh Pabba[c], Robert W. Cohn[c], Gareth H. McKinley[a]

[a] *Department of Mechanical Engineering, Massachusetts Institute of Technology, Cambridge, Massachusetts 02139*
[b] *Department of Mathematics, Massachusetts Institute of Technology, Cambridge, Massachusetts 02139*
[c] *ElectroOptics Research Institute & Nanotechnology Center, University of Louisville, Louisville, Kentucky 40292*

Abstract

Recent experiments have shown that it is possible to self-assemble very uniform polymeric microfibers and nanofibers by exploiting elasto-capillary thinning of macroscopic liquid bridges (Harfenist et al., Nano Lett., 4(10), 2004). We develop a model of this process that describes the simultaneous visco-elasto-capillary thinning and drying of polymeric liquid filaments. A one-dimensional formulation is developed using a slender body approximation to the inertialess equations of motion. The evolution in the kinematics, stress and composition of differential material elements are computed by numerical simulation on a fixed mesh using an explicit Eulerian scheme. The polymer rheology is described by a single-mode Giesekus model with an experimentally-determined concentration-dependent shift factor that accounts for compositional dependence of the zero shear rate viscosity and the relaxation time of the fluid. The numerical simulations are compared to capillary break-up extensional rheometer (CABER) experiments using high molecular weight poly(methyl methacrylate) solutions in chlorobenzene with a range of mass fractions in the concentrated regime. Very large reductions in the radius of the thinning thread - spanning two to three orders of magnitude - are attainable by careful control of the mass transfer rate, the molecular extensibility of the dissolved polymer and the dynamics of the elasto-capillary thinning process. Simulations show that the fiber formation process can be conveniently parameterized by two dimensionless parameters which compare, respectively, the rate of capillary thinning with the rate of elastic stress relaxation and with the rate of solvent evaporation.

Key words: capillary thinning, microfiber, nanofiber, extensional rheology, CABER.

*Corresponding author. E-mail address: jerome.crest@polytechnique.edu

1. Introduction

The fabrication of microscale and nanoscale polymer fibers has gained considerable interest because of its potential applications in nano-electronics [1], nano-sensors [2], low-loss optical wave guides [3]. Other applications in fields such as filtration and biotechnology have been summarized in the review by Huang et al. [4]. Common fiber-forming processes do not allow precise, controlled placement of individual submicron fibers on a substrate. In melt spinning, dry spinning or wet spinning [5], the extrusion of the polymer melt or solution is unidirectional and leads typically to fibers with diameter ranging from tens of microns to millimeters. Only electrospinning readily produces submicron diameter fibers, which are generally collected as non-woven mats and thus cannot be arranged in controlled patterns. Recently, various microfabrication techniques for producing controlled networks of fibers have been reported by Harfenist et al. [6], Berry et al. [7] and Nain et al. [8, 9]. Exploiting capillary thinning of macroscopic liquid threads, they managed to place individual microfibers and nanofibers in a controlled way on a substrate. In this study, we focus on the "Brush-On" fabrication method, presented in Fig. 1, which can be used to form suspended structure-spanning fiber bridges on MEMS devices. In Fig. 1(a), an applicator spreads a large sheet of polymer solution over an array of micropillars by a smooth unidirectional brushing motion. In Fig. 1(b), this sheet breaks up into individual threads that bridge neighboring pillars, in the direction of brushing. Based on the observed uniformity of arrays of fibers it appears that similar amounts of liquid wet each pair of pillars. The resulting liquid bridges, suspended between two micropillars, undergo simultaneous capillary thinning and evaporation of the solvent, forming fibers much thinner than the dimensions of the micropillars, as shown in Fig. 1(c). The present paper focuses on this later stage of capillary thinning between two micropillars, which appears to be the critical feature in the formation of nanoscale air-suspended fiber bridges. We do not attempt to describe the initial stages of brushing that leads to the breakup of the sheet and formation of an array of liquid bridges.

The action of capillary forces on the liquid bridge results in an extensional flow between two fixed plates. The fluid dynamics of those extensional flows has been studied extensively utilizing the Capillary Breakup Extensional Rheometer (CABER), introduced in 1990 by Bazilevsky et al. [10]. In a filament

thinning device, a liquid bridge is formed between two circular plates, which are rapidly separated and then held at a fixed axial separation. The evolution of the midfilament diameter is monitored with a laser micrometer during the process of necking until a final equilibrium thread radius is achieved or the filament breaks.

Simultaneous elasto-capillary thinning and mass transfer has been studied by Tripathi et al. [11] to characterize the processability of adhesives and other non-Newtonian fluids. The effects of combined heat and mass transfer in extensional flows has also been studied extensively during the dry spinning process [12, 13]. In the present work, we develop a model that describes the simultaneous visco-elasto-capillary thinning and drying of cylindrical filaments of polymer solutions. Our goal is to understand how the balance of forces evolves during the thinning process in order to obtain the thinnest and most uniform fibers possible. Very large radius reductions, spanning two to three orders of magnitude, are attainable by careful control of the mass transfer rate and the elasto-capillary thinning dynamics. The model, based on a one-dimensional slender body theory is presented in Section 2. In Section 3, rheological and physical characterization of PMMA in chlorobenzene solutions at different concentrations are presented. Section 4 presents the methods used in the numerical simulations. The last section explains the dynamics of capillary thinning with drying, then compares simulation and experiments at the macroscopic scale using CABER experiments. Finally, we use our model to predict the possible outcome of "Brush-On" experiments at the nano and micro scale and we provide guidelines to "design" polymer solutions leading to controlled radius reduction in the thinning thread.

2. Model

2.1. Problem statement

In a "Brush-On" experiment, the liquid bridge is suspended between the top of two micropillars. For the sake of simplicity, we assume that at this contact point the "foot" of the thread is cylindrical due to capillarity. The model system presented in Fig. 2 shows an axisymmetric liquid bridge of a polymer solution of constant density ρ constrained between two circular disks of radii R_0 and initial separation L_i. The initial aspect ratio of the liquid bridge is then defined as $\Lambda_i = L_i/R_0$. It is surrounded by ambient air at rest at 23°C and the flow is assumed to remain isothermal throughout. The surface

tension σ of the liquid-air interface is spatially uniform and, for simplicity, is assumed to be independent of the mass fraction of the binary mixture. It is certainly straightforward to incorporate a concentration dependent surface tension, however such effects are small compared to the large (exponential) changes in the bulk rheology, and inhibit our understanding of the basic physics. The solvent Newtonian viscosity is noted η_s. The zero shear rate viscosity of the polymer $\eta_{p0}(x)$, the relaxation time $\lambda(x)$, the total zero shear rate viscosity $\eta_0(x) = \eta_s + \eta_{p0}(x)$, are strong functions of the mass fraction x of the high molecular weight polymer in solution. The zero shear rate viscosity and relaxation time at the initial mass fraction x_0 are respectively noted $\eta_{00} = \eta_0(x = x_0)$ and $\lambda_0 = \lambda(x = x_0)$. The "Brush-On" process is modeled by giving the top plate a fast vertical displacement, illustrated schematically in Fig. 2(b) until the final length L_0 (corresponding to the aspect ratio Λ_0). This step strain is modeled in Section 2.4 using a lubrication approximation. Our model and numerical simulation are valid after this step strain and describe the self-thinning of the liquid bridge between two fixed plates, illustrated in Fig. 2(c) and Fig. 2(d). The parameter R_{mid} represents the radius at the midfilament $z = \Lambda_0/2$. The fluid column is assumed to remain axi-symmetric. Shearing forces are caused at the beginning of the deformation by the no-slip boundary condition along the upper and lower solid surfaces. As the filament becomes long and slender, the flow tends toward an ideal uniaxial elongational deformation and shearing effects are negligible. The shear thinning behavior of the working fluid is thus neglected.

In this study, the small size of the initial sample and the large viscous and elastic contributions to the total force ensure that gravitational body forces and inertia are negligible at all strains. This inertialess regime leads to an axially symmetric profile about the midplane of the filament. The physical problem is formulated in a cylindrical coordinate system with its origin located at the center of the bottom disk. For the axisymmetric situations of interest in this work, the problem does not depend on the azimuthal coordinate. The aspect ratio $\Lambda_0 = L_0/R_0$ being a large parameter, a slender body approximation is used to reduce by one the spatial order of the 2-D mathematical problem [14, 15]. The kinematics of the motion is therefore essentially one-dimensional, and all variables can be averaged on a cross section and regarded as functions of the position z and the time t. The limits of this approximation compared to a full two-dimensional axisymmetric description of the capillary thinning process in non-Newtonian fluids has been studied by Yildrim et al. [16] and Yao et al. [17].

2.2. Governing equations

Under the assumption of a slender inertialess jet, the mass and the momentum conservation laws can be considerably simplified [18, 19]. To non-dimensionalize the governing equations, we select the radius of the end-plates R_0 as a characteristic length, and the visco-capillary time scale $t_{cap0} = \eta_{00} R_0/\sigma$ as a characteristic time for evolution of the thread. This leads to the following dimensionless variables: $z^* = z/R_0$, $\underline{\mathbf{v}}^* = \underline{\mathbf{v}}/(R_0/t_{cap0})$, $t^* = t/t_{cap0}$, $\underline{\underline{\mathbf{\Pi}}}^* = \underline{\underline{\mathbf{\Pi}}}/(\sigma/R_0)$, where $\underline{\underline{\mathbf{\Pi}}}$ is the stress in the fluid. Four dimensionless groups can be identified in this problem; one describing the initial geometry of the thread, one comparing the solvent viscosity to the total viscosity of the solution, and two describing the fluid dynamics of the process itself:

Aspect ratio of the liquid bridge: $\Lambda_0 = L_0/R_0$

Initial solvent viscosity ratio: $\beta_s = t_{capS}/t_{cap0} = \eta_s/\eta_{00}$

Elasto-capillary number: $Ec_0 = \lambda_0/t_{cap0} = \lambda_0\sigma/\eta_{00}R_0$

Processability number: $P_0 = t_{cap0}/t_{evap0} = h_m\eta_{00}/\sigma$

The elasto-capillary number compares the relaxation time of the polymer solution λ_0 at the initial mass fraction x_0 to the visco-capillary time scale t_{cap0}. It can thus also be understood as a Deborah number, in which the extension rate of the self-thinning scales like the inverse of the visco-capillary time. The parameter β_s compares the visco-capillary time scale of the solvent $t_{capS} = \eta_s R_0/\sigma$ to that of the polymer solution $t_{cap0} = \eta_{00} R_0/\sigma$. A more extensive discussion of these two dimensionless groups can be found in the review by McKinley [20]. The processability number, defined by Tripathi et al. [11], compares the evaporation time scale $t_{evap0} = R_0/h_m$, where h_m is a mass transfer coefficient (with S.I. units of m/s), to the visco-capillary time scale of the polymer solution, t_{cap0}. These variables along with the dimensionless parameters are used in developing the non-dimensional governing equations and boundary conditions given in the next section. For convenience, we drop the asterisk notation in the remainder of the paper and do not explicitly identify variables as dimensionless. We denote the dimensionless

spatially and temporally evolving radius as $h(z,t) = R(z,t)/R_0$.

2.2.1. Continuity equations

During the filament thinning process the volatile solvent component evaporates from the solution and we thus need to distinguish between the two species in the continuity equations. The mass balance for the polymer on a control volume delimited by the cross sections between z and $z + dz$ gives:

$$\frac{\partial(h^2 x)}{\partial t} + \frac{\partial(v h^2 x)}{\partial z} = 0 \tag{1}$$

where $v(z,t)$ is the axial velocity and $x(z,t)$ is the mass fraction of polymer in each slice.

For the evaporating solvent, an additional term describing mass transfer at the air-liquid interface appears in the continuity equation. The thinning process occurs under ambient condition and does not involve forced convection (e.g. by blowing air over the filament). Convective mass transfer is thus negligible and it is assumed that the process is controlled by diffusion of the solvent in both the viscous liquid phase and the gas phase. Fig. 3 shows a schematic of the transient diffusion problem in the cylinder. We denote by $x_s(r,z,t)$ the local mass fraction of solvent in the system. The parameter x, introduced earlier, is the average mass fraction of polymer over a cross section. In the liquid phase, the diffusion coefficient $D_{sl}(x_s)$ is a strong function of the remaining mass fraction of solvent x_s in the increasingly viscous polymer solution. The driving force for radial diffusion is $x^l_{s,0} - x^l_{s,i}$, i.e. the difference between the mass fraction of solvent at the centerline and at the interface. In the gas phase, the diffusion coefficient D_{sg} is taken to be independent of the mass fraction of solvent and the driving force is $x^g_{s,i} - x^g_{s,\infty}$, i.e. the difference between mass fraction of solvent at the interface and in the ambient air far from the filament. In our study, non aqueous solvents are used and $x^g_{s,\infty} = 0$. Assuming thermodynamic equilibrium at the interface liquid-air, we can relate the mass fraction of solvent at the interface in the liquid and gas phase using Raoult's law (polymer-solvent interactions were found to have little effect on the system). When combined with Dalton's law this gives:

$$x^l_{s,i} = \frac{p_{s0}}{p} x^g_{s,i} = \alpha_p x^g_{s,i} \tag{2}$$

where p_{s0} is the vapor pressure of solvent at 23°C and p is the atmospheric pressure. The dimensionless parameter $\alpha_p = \frac{p_{s0}}{p}$ is the partition coefficient. To describe the mass transfer process of the evaporating

solvent, we use the two-film resistance theory proposed by Lewis and Whitman in 1924 [21]. We can define a mass transfer coefficient for the liquid phase h_l and for the gas phase h_g so that the mass flux of solvent $\dot{m}_s$ is:

$$\dot{m}_s = \rho h_l (x^l_{s,0} - x^l_{s,i}) \tag{3}$$

$$\dot{m}_s = \rho h_g x^g_{s,i} \tag{4}$$

Calling δ_l and δ_g respectively the boundary layer in the liquid and the gas, and noting that when diffusion in the liquid is fully developed $\delta_l = R$, the mass transfer coefficients scale as:

$$h_l \approx \max\left(\frac{D_{sl}(x_s)}{\delta_l}, \frac{D_{sl}(x_s)}{R}\right) \approx \max\left(\sqrt{\frac{D_{sl}(x_s)}{t}}, \frac{D_{sl}(x_s)}{R}\right) \tag{5}$$

$$h_g \approx \frac{D_{sg}}{\delta_g} \approx \sqrt{\frac{D_{sg}}{t}} \tag{6}$$

We can compute an average mass transfer coefficient h_m based on the driving force $x^l_{s,0} - \alpha_p x^g_{s,\infty}$ (which simplifies to $x^l_{s,0}$ since $x^g_{s,\infty} = 0$). This gives:

$$\frac{1}{h_m} = \frac{1}{\alpha_p h_g} + \frac{1}{h_l} \tag{7}$$

Depending on the length scale and the value of the diffusion coefficient, the resistance in the liquid or the gas may dominate, but this theory covers both limiting cases. The mass transfer coefficient h_m depends on time as the filament shrinks and the solvent evaporates.

Finally, the total evaporative flux per unit length of a slice of filament with radius $R(t)$ can be written $\dot{m} = 2\pi\rho R h_m(1-x)$. In dimensionless form, the continuity equation for the solvent gives:

$$\frac{\partial(h^2(1-x))}{\partial t} + \frac{\partial(vh^2(1-x))}{\partial z} + 2hP_0(1-x) = 0 \tag{8}$$

where $P_0 = t_{cap0}/t_{evap0} = h_m\eta_{00}/\sigma$ is the processability number, which compares the rate of evaporation to the rate of visco-capillary thinning in the filament. The mass transfer theory we developed will be used in Section 5.1 to predict the order of magnitude of the average mass transfer coefficient h_m.

2.2.2. Equation of motion

The axial force balance integrated over the control volume delimited by the cross sections between z and $z + dz$ gives:

$$\frac{\partial}{\partial z}\left\{h^2\left[\frac{1}{h(1+h_{,z}^2)^{\frac{1}{2}}}+\frac{h_{,zz}}{(1+h_{,z}^2)^{\frac{3}{2}}}\right]+h^2(T_{zz}-T_{rr})\right\}=0 \tag{9}$$

where $\kappa = \frac{1}{h(1+h_{,z}^2)^{\frac{1}{2}}}+\frac{h_{,zz}}{(1+h_{,z}^2)^{\frac{3}{2}}}$ is the dimensionless mean curvature of the interface ($h_{,z}$ and $h_{,zz}$ denote respectively the first and second partial derivative of the radius with respect to the axial coordinate). The first term represents the capillary force at the liquid interface while the second represents the force contribution from the solvent and the polymer. Here $T_{zz}(z,t)$ and $T_{rr}(z,t)$ denote respectively the average axial and radial component of the extra stress tensor in each slice. A detailed derivation of Eq. (9) can be found in the review by Eggers [22]. The capillary term includes the full mean curvature κ. As shown by Papageorgiou [15], keeping the full curvature term in Eq. (9) is not formally asymptotically correct. However, several authors [16, 18] have also adopted this approach. The main reason for retaining the full curvature term is that the resulting set of 1-D equations then predicts the equilibrium shapes of static bridges exactly.

We separate the solvent contribution $\underline{\underline{\boldsymbol{T}}}^{\boldsymbol{s}}$ and the polymer contribution $\underline{\underline{\boldsymbol{T}}}^{\boldsymbol{p}}$ in the extra stress tensor:

$$\underline{\underline{\boldsymbol{T}}} = \underline{\underline{\boldsymbol{T}}}^{\boldsymbol{s}} + \underline{\underline{\boldsymbol{T}}}^{\boldsymbol{p}} \tag{10}$$

The Newtonian solvent stress difference for an extensional flow can be expressed as:

$$T_{zz}^s - T_{rr}^s = 3\eta_s \frac{\partial v}{\partial z} \tag{11}$$

where $3\eta_s$ is the extensional viscosity or Trouton viscosity of the Newtonian solvent.

The final expression of Eq. (9) can then be written:

$$\frac{\partial}{\partial z}\left[3\beta_s h^2\frac{\partial v}{\partial z}+\frac{h}{(1+h_{,z}^2)^{\frac{1}{2}}}+\frac{h^2 h_{,zz}}{(1+h_{,z}^2)^{\frac{3}{2}}}+h^2(T_{zz}^p-T_{rr}^p)\right]=0 \tag{12}$$

The sum of the terms in the square brackets can be identified as the tensile force in the filament. In the inertialess regime, this tensile force is uniform along the axial coordinate and depends only on time. It

has three contributions, a Newtonian solvent stress, a capillary stress and a non-Newtonian polymeric stress difference arising from the stretching of the polymeric chains.

The boundary conditions for this problem are two fixed plates imposing $v = 0$ at $z = 0$ and at $z = \Lambda_0$. Because of the slender body approximation, the radial no-slip condition cannot be satisfied exactly at the end plates. However, numerical studies show this does not affect the determination of the thinning dynamics in the central portion of the filament significantly [16, 17]. The initial conditions are $T^p_{zz} = T^p_{rr} = 0$, $x = x_0$ at $t = 0$. The computation of the initial profile is described in Section 2.4. The initial velocity profile is computed by solving Eq. (12), in conjunction with the initial shape of the filament.

2.3. Constitutive equations

To describe the viscoelastic contribution to the stress in concentrated polymer solutions, we use a single-mode Giesekus model [23], in which the relaxation time and viscosity are allowed to depend on concentration. We choose a single relaxation time for simplicity; a detailed comparison of the dynamics with a spectrum of relaxation times in the absence of solvent evaporation has been provided by Yao et al. [17]. The elastic stresses are governed by the following partial differential equations (in dimensionless form):

$$T^p_{zz} + Ec_0\frac{\lambda(x)}{\lambda_0}\left(\frac{\partial T^p_{zz}}{\partial t} + v\frac{\partial T^p_{zz}}{\partial z} - 2\frac{\partial v}{\partial z}T^p_{zz}\right) + \frac{\lambda(x)}{\lambda_0}\frac{\eta_{00}}{\eta_{p0}(x)}\beta^{-1}\alpha Ec_0(T^p_{zz})^2 = 2\beta\frac{\eta_{p0}(x)}{\eta_{00}}\frac{\partial v}{\partial z} \tag{13}$$

$$T^p_{rr} + Ec_0\frac{\lambda(x)}{\lambda_0}\left(\frac{\partial T^p_{rr}}{\partial t} + v\frac{\partial T^p_{rr}}{\partial z} + \frac{\partial v}{\partial z}T^p_{rr}\right) + \frac{\lambda(x)}{\lambda_0}\frac{\eta_{00}}{\eta_{p0}(x)}\beta^{-1}\alpha Ec_0(T^p_{rr})^2 = -\beta\frac{\eta_{p0}(x)}{\eta_{00}}\frac{\partial v}{\partial z} \tag{14}$$

where the parameter β is defined by $\beta = 1 - \beta_s$. The positive dimensionless parameter α is called the mobility factor and is associated with the anisotropy of the hydrodynamic drag on the constituent polymer molecules. The initial elasto-capillary number is defined by $Ec_0 = \lambda_0\sigma/\eta_{00}R_0$, where $\lambda_0 = \lambda(x = x_0)$, $\eta_{00} = \eta_0(x = x_0)$. In the case of very low solvent viscosity compared to polymer viscosity ($\beta_s << 1$), we can approximate the polymer viscosity with the solution viscosity $\eta_{p0}(x) \approx \eta_0(x)$ in the constitutive equations. For $\alpha = 0$, we recover the quasi-linear Oldroyd-B model. The non-linear

quadratic term in stress introduced by the Giesekus model is necessary to describe finite time break-up of liquid bridges between two plates. As shown by Entov & Hinch [24] elasto-capillary thinning in the Oldroyd-B model leads to an exponential decrease of the radius with time, but cannot capture break-up.

2.4. Modeling of the initial filament

We model the initial displacement of the fluid drop to form a liquid bridge by a lubrication analysis based on the reversed squeeze flow problem for a Newtonian fluid. This problem has already been used in extensional rheometry by Spiegelberg et al. [25] and Bach et al. [26] and is a good approximation for small deformations, even for non-Newtonian fluids. We choose a reference set of Lagragian points Z_0, initially located on a cylindrical free surface of dimensionless radius $h(t = 0, z) = 1$. The initial aspect ratio is Λ_i. The particle coordinates (R_{lub}, Z_{lub}) at the final aspect ratio Λ_0 can be computed using most readily a Lagrangian formulation, giving the following dimensionless expressions for the coordinates locations in the lower half of the fiber ($Z_0 \in \left[0, \frac{1}{2}\right]$):

$$Z_{lub} = \frac{\Lambda_i}{2}\left[1 - \left(\frac{(2Z_0 - 1)^2}{(2Z_0 - 1)^2 + 4Z_0(1 - Z_0)e^{-\epsilon}}\right)^{\frac{1}{2}}\right] e^{\epsilon} \tag{15}$$

$$R_{lub} = \left[(2Z_0 - 1)^2 - 4Z_0(Z_0 - 1)e^{-\epsilon}\right]^{\frac{3}{4}} \tag{16}$$

The shape of the upper half of the fiber is given by symmetry. In this expression ϵ represents the Hencky strain. To compute the profile obtained for an imposed aspect ratio Λ_0 we have to choose $\epsilon = \ln(\Lambda_0/\Lambda_i)$. To compute the profile on the Eulerian mesh described in Section 4, Eq. (15) is inverted analytically and substituted into Eq. (16) to obtain a function of the form $R_{lub} = f(Z_{lub})$.

3. Fluid characterization

3.1. Concentrated solutions of PMMA in chlorobenzene

Poly(methyl methacrylate) (PMMA), an amorphous thermoplastic polymer is used in all the experiments (Sigma-Aldrich, CAS number 9011-14-7). The average molecular weight is $\overline{M}_w = 996$ kg/mol. A polydispersity index of $\overline{M}_w/\overline{M}_n = 2.5$ is determined with a Waters Gel Permeation Chromatograph. The polymer is dissolved in chlorobenzene, a good solvent, and solutions with initial polymer mass

fractions $0.1 < x_0 < 0.35$ are prepared. The intrinsic viscosity $[\eta]$ can be related to the molecular weight $\overline{M}_w$ of a linear polymer by the Mark-Houwink equation $[\eta] = K\overline{M}_w^a$, where the constants K and a depend on the polymer, solvent and temperature. In the literature [27], data is available for PMMA in benzene at 25°C: $K = 5.2 \times 10^{-6}$ m^3/kg and $a = 0.76$ (corresponding to good solvent conditions). We assume that the same parameters can be used for our chlorobenzene based system. This leads to $[\eta] = 0.188$ m^3/kg for our molecular weight. We define the concentration of polymer as $c = \rho x$, where ρ is the density of the polymer solution (which is taken to be independent of concentration). The critical chain overlap concentration c^* is the crossover concentration between the dilute and the semidilute concentration regimes. Physically, the critical chain overlap concentration is the point at which the self-concentration inside a single macromolecular chain equals the solution concentration and can be expressed as [28]:

$$c^* = 0.77/[\eta] = 4.1 \times 10^{-3} \text{ g/cm}^3 \tag{17}$$

This corresponds to an overlap mass fraction $x^* = 0.004$. If the concentration is further increased, we reach the semidilute entangled regime. The crossover of concentration from the semidilute unentangled to semidilute entangled regime is referred to as the critical entanglement concentration, c_e. In other words, c_e marks the distinct onset of significant chain entanglements in solution. Graessley [29] reports that the entanglement mass fraction is defined by $x_e = \left(\overline{M}_w/(M_e)_{melt}\right)^{-1/1.3}$, where $(M_e)_{melt} = 7000$ g/mol is the entanglement molecular weight of a PMMA melt, which leads to $x_e = 2.2$ wt.% for our system. The lowest initial mass fraction of $x_0 = 0.1$ used in this study is more than twenty times the overlap concentration and five times the entanglement concentration, which means that all solutions studied are fully in the concentrated regime. In these concentrated solutions, the entanglement network steadily evolves over the course of solvent evaporation. At early times the solution has a moderate viscosity and low elasticity because the density of entanglements is small at high solvent concentrations. As the solvent evaporates, the viscosity and relaxation time increase, according to an exponential law that is determined in Section 3.2. At a critical concentration, the random diffusive motion of the chains is dramatically decreased and the material undergoes a glass transition. The final state of the system is a glassy solid.

The surface tension of the solutions was measured using the Wilhelmy technique. An average surface tension over all mass fractions of $\sigma = 0.04$ N/m was determined.

3.2. Shear rheology

The rheology of the test fluids in both steady and dynamic shear flow was investigated at 23°C using an ARG2 rheometer from TA Instruments. 20 mm and 60 mm cone-and-plate fixtures were used at mass fractions $x_0 > 0.18$; a double concentric gap Couette geometry was used at lower concentrations. Since chlorobenzene is a volatile solvent with low viscosity, a solvent trap was used to avoid drying.

3.2.1. Steady shear

In Fig. 4(a), we present the steady shear viscosity $\eta(\dot{\gamma})$ versus shear rate for solutions of PMMA in chlorobenzene with initial mass fractions in the range $0.1 < x_0 < 0.35$. At all concentrations, shear thinning behavior is observed. This is initially weak at low concentrations and becomes stronger as concentration increases. In Fig. 3(b), the steady shear data is collapsed on a master curve using time-concentration superposition [29], with a common shift factor a_c for vertical and horizontal shifting. The reference state for shifting is the experiment at $x_0 = 0.2$. In the inset of Fig. 4(b), the zero shear rate viscosity $\eta_0(x)$ is plotted against mass fraction. The data is well fitted by an exponential relationship $a_c = \eta_0(x)/\eta_{00} = e^{36(x-x_0)}$. A similar scaling was found by Bornside et al. [30]. The zero shear rate viscosity increases dramatically with concentration and spans about four order of magnitude from $x_0 = 0.1$ to $x_0 = 0.35$. The viscosity of pure chlorobenzene was found to have the value $\eta_s = 0.8 \times 10^{-3}$ Pa s. In dilute or semidilute solutions, the anistropic drag coefficient α appearing in the Giesekus model is a strong function of mass fraction. For the concentrated solutions used in this study, the parameter α is determined by fitting the transition to shear-thinning in the steady shear viscosity data [31]. A weak dependence on mass fraction is found and an averaged coefficient over all concentrations of $\alpha = 10^{-4}$ is computed. The steady shear viscosity predicted by the Giesekus model with $\alpha = 10^{-4}$ is represented with a black line in Fig. 4(b) and provides a good description of the fluid rheology for $0.1 \leq x_0 \leq 0.35$. The more gradual transition to shear-thinning observed in the experiments is a reflection of the relaxation time spectrum in the fluid. This is further discussed in the next section.

3.2.2. Small Amplitude Oscillatory Shear

In order to independently determine the relaxation time scaling with concentration, Small Amplitude Oscillatory Shear (SAOS) tests were also performed at 23°C. The storage modulus $G'(\omega)$ and the relaxation modulus $G''(\omega)$ data are reported respectively in Fig. 5(a) and Fig. 5(b). The data is collapsed on a master curve in Fig. 5(c) and Fig. 5(d) using time-concentration superposition and a reference concentration of $x_0 = 0.2$. The data is fitted to a generalized Maxwell model with 6 modes and an average relaxation time is then calculated for each concentration as following (see reference [32] for more details):

$$\lambda(x) = \frac{\sum_k G_k(x)\lambda_k^2(x)}{\sum_k G_k(x)\lambda_k(x)} \tag{18}$$

where G_k is the shear modulus of the k^{th} mode and λ_k the relaxation time of the k^{th} mode. The relaxation time as a function of mass fraction is presented in Fig. 6. The data can be fitted to the exponential law $\lambda(x)/\lambda_0 = e^{31(x-x_0)}$ with $\lambda_0 = 15$ ms at $x_0 = 0.2$. This means that the fluid relaxation time increases by several orders of magnitude during the evaporation of the solvent. The shear modulus $\frac{G}{G_0} = \frac{\eta_0}{\eta_{00}}\frac{\lambda_0}{\lambda} = e^{5(x-x_0)}$ is found to increase exponentially with concentration. Kinetic theory predicts that for concentrated solutions, $\frac{G}{G_0} = \left(\frac{x}{x_0}\right)^2$ [29]. We compared those two scalings and we observed that they have numerical values of the same order of magnitude at mass fractions $x \leq 0.8$, which is the range of concentrations relevant for our study.

3.3. Mass transfer

We can compare the relative resistance of the liquid phase and the gas phase during the diffusion process of chlorobenzene using the theory developed in Section 2.2. The diffusion coefficient for PMMA in chlorobenzene as a function of the polymer mass fraction x is reported in a paper by Bornside et al. [30]:

$$D_{sl} = (7.24 \times 10^{-11}\ \mathrm{m}^2/\mathrm{s})\ \exp\left(-\frac{0.240}{0.0277 + (1-x)^{2.19}}\right) \tag{19}$$

In Section 5.4 we show that the thinning dynamics do not vary strongly at polymer mass fractions $x > 0.5$ because the flow is arrested and dominated solely by the diffusive mass transfer. All the scalings

derived in this section thus focus on the regime $x < 0.5$. Within this range of mass fractions, the diffusion coefficient in the liquid phase D_{sl} given by Eq. 19 shows a plateau and we pick an average value $\overline{D}_{sl} \approx 5 \times 10^{-11}$ m^2/s. Both the liquid side and the vapor side of the interface may exhibit significant resistance to mass transfer depending on the length scale and time scale of the capillary thinning process. Their resistance varies with time as the solvent evaporates and the filament thins. Transient diffusion of solvent through the liquid phase dominates at short times $t \leq R^2/\overline{D}_{sl}$, which is of the order of 200 s for $R \approx 100$ μm and of 2 s for $R \approx 10$ μm. For the PMMA/chlorobenzene system, the relative resistance of the liquid phase compared to the gas phase during the transient diffusion process can be evaluated from Eq. 7 and Table 1 to be $\alpha_p h_g/h_l \approx \alpha_p \sqrt{D_{sg}/\overline{D}_{sl}} \approx 6$. Thus the resistance dominates on the liquid side. Neglecting the gas resistance, from Eq. 5 a mass transfer coefficient $h_m \approx \sqrt{\frac{\overline{D}_{sl}}{t}}$ is a good approximation at times $t \leq R^2/\overline{D}_{sl}$ and this value does not change much over the typical time scale of the experiments. Exploratory calculations show that at later times the mass transfer coefficient is also only a weak function of time. For the sake of simplicity and to enable us to focus more on the fluid dynamics of the process rather than mass transfer dynamics, we pick an average value $\overline{h}_m$ independent of time, which is determined by matching experimental results from capillary thinning with numerical simulations (Section 5.1).

3.4. Glass transition of the PMMA/chlorobenzene solution

Using the Kelley–Bueche equation [33], we can estimate the mass fraction x_g at which the glass transition occurs at 23°C:

$$T_g = \frac{R_K x_g T_{g2} + (1 - x_g) T_{g1}}{R_K x_g + (1 - x_g)} = 23^\circ\text{C} \Rightarrow x_g = 0.85 \tag{20}$$

where T_{g1} and T_{g2} are respectively the glass transition temperature of PMMA and chlorobenzene (reported in Table 1), and $R_K = \alpha_2/\alpha_1$, where α_i is the difference in thermal expansivity between liquid and glass for each component. A value of $R_K = 2.5$ is calculated for the PMMA/chlorobenzene system. Our rheological characterizations show that in the range of polymer mass fractions $0.1 \leq x \leq 0.35$, the correlations for viscosity and relaxation time with concentration are well described using exponential laws. However, close to the glass transition, both the viscosity and the molecular relaxation time are

expected to begin to diverge. This effect can be attributed to a decrease in free volume described by the generalized Doolittle equation [34, 35]. Accurate description of this (super-exponential) increase in these viscometric properties requires careful rheological measurements near T_g. As we describe in Section 5.4, the convective axial flow and drainage of fluid becomes negligible compared to the volume decrease by solvent evaporation for $x > 0.5$. Thus the dynamics of the elasto-capillary thinning are not strongly affected by the specific correlations chosen for viscosities and relaxation times at mass fractions in the range $0.5 \leq x \leq 0.85$. In the present study, we therefore simply extrapolate the exponential correlations in $\lambda(x)$ and $\eta_0(x)$ at all concentrations, which underestimates the viscoelastic properties of the solution close to the glass transition.

4. Numerical simulation

We use a fixed mesh of 400 points distributed over half of the symmetric fiber and solve the equations in an Eulerian frame using finite differences. The other half of the fiber is given by symmetry. The mesh size resolution is denoted Δz and the time-step Δt. For the time discretization, our strategy is to advance Eq. (1), Eq. (8), Eq. (13) and Eq. (14) by convex combination of Euler steps, defined in [36] to obtain a 3^{rd} order Runge-Kutta TVD (total-variation-diminishing) update. Then the elliptic constraint of Eq. (12) is solved to extract the velocity. For the spatial discretization, we use a centered difference scheme for the elliptic constraint in Eq. (12). With Dirichlet boundary conditions $v(z = 0) = 0$ and symmetry at $z = \Lambda_0/2$, this discretization give rise to a tri-diagonal system of equations that can be inverted using standard Gaussian elimination. The convective derivatives are evaluated using a WENO [37] scheme, and all other spatial derivatives are discretized using a standard centered difference scheme. The numerical procedure is second order accurate in space, and stable for $\Delta t \leq C\beta_s \Delta z^2$, for some constant C. In the present study, $\beta_s = \eta_s/\eta_{00}$ ranges from 10^{-2} to 10^{-6} over the mass fractions used experimentally. This imposes very small time-steps conditions to satisfy numerical stability. From a physical point of view, the solvent viscosity is so low compared to the total solution viscosity that it has a negligible contribution in the force balance, as demonstrated in Section 5.3. As long as we keep the relative contribution of the solvent stress negligible, we can choose an arbitrary value of β_s to decrease the computational time. A value of $\beta_s = 5 \times 10^{-2}$ is chosen and is used in all numerical simulations.

The slender body approximation prevents us from imposing directly the no-slip boundary condition at the endplates. Several methods are reported in the literature to reduce the resulting apparent slip at the endplates while keeping the same thinning dynamics. Tuck et al. [38] defined an increased viscosity at the boundary to match the lubrication solution of the reversed squeeze flow. In the present study, we impose a zero strain rate at the endplates ($\partial v/\partial z = 0$ at $z = 0$). This results in a local jump in strain rate at the first mesh points in the filament close to the endplates but reduces significantly the slip velocity while not appreciably affecting the dynamics at the midfilament (see reference [32] for more details).

5. Results and discussion

5.1. Experimental determination of the average mass transfer coefficient

Capillary thinning experiments for various mass fractions of PMMA in chlorobenzene were performed using a CABER instrument (Cambridge Polymer Group). The diameter at the midfilament $2R_{mid}(t)$ is tracked using a laser micrometer which measures the size of an object in its path based on the intensity of light entering the sensing element. The initial length of the liquid bridge (see Fig. 2) is $L_i = 2$ mm and the radius of the plates $R_0 = 3$ mm. The final length of the liquid bridge following stretching is $L_0 = 10$ mm corresponding to an aspect ratio of $\Lambda_0 = 3.3$. Quantitative comparisons between the CABER experiments and numerical simulations are presented in Fig. 7 and the simulation parameters are reported in Table 2. An average mass transfer coefficient $\overline{h}_m = 6.5 \times 10^{-6}$ m/s independent of concentration and time is determined by fitting the numerical simulations to the experimental data. This value is consistent with the model presented in Section 3.3. On the length scales and time scales of the CABER experiment, the diffusive boundary layer is never fully developed and $\overline{h}_m \approx h_l \approx \sqrt{\frac{\overline{D}_{sl}}{t_{exp}}}$, where t_{exp} is the typical time scale of the experiment. For $1 < t_{exp} < 10$ s we find that $10^{-6} < \overline{h}_m < 10^{-5}$ m/s. At high mass fractions, for $0.24 < x_0 < 0.28$, the experimental data cannot be plotted over the whole time of the experiment because the long drainage time ($t_{cap_0} \approx 3$ s) leads to gravitational sagging and loss of top/bottom symmetry, before equilibrium is reached. At the initial mass fraction $x_0 = 0.22$, the behavior at early times is well described by our model. A fast drying is observed experimentally at intermediate times, which does not change quite as abruptly for the simulation. This is due to the

simplicity of our mass transfer model. A complete description of the mass and heat transfer dynamics in two dimensions would be required for a fully quantitative comparison. At mass fraction $x_0 = 0.22$, the laser micrometer data from CABER does not show the formation of a fiber. Videomicroscopy images of the experiment reveal that a very thin fiber is formed but is rapidly broken at the junction of the upper quiescent reservoir by air perturbation. A sequence of shapes of the filament during a CABER experiment is compared to numerical simulation results in Fig. 8 for an initial mass fraction $x_0 = 0.24$. Very good qualitative agreement of the evolution in the axial filament profile a function of time is observed.

5.2. Kinematics

In Fig. 9 we show a range of numerical simulations of the CABER experiment for a fixed aspect ratio $\Lambda_0 = 3.3$ and fixed solvent viscosity ratio $\beta_s = 0.05$. A sequence of profiles is represented as a function of dimensionless time. In the case of a Newtonian fluid with no drying ($Ec_0 = 0$, $P_0 = 0$), capillary thinning leads to a rapid breakup at time $t \approx 4.7$. The numerical simulation resolves a radius reduction of $h \approx 10^{-3}$ before becoming numerically unstable. For PMMA/chlorobenzene solutions of initial mass fractions $x_0 = 0.26$ or $x_0 = 0.22$ (with simulation parameters as reported in Table 2), we see that a new equilibrium configuration is reached before breakup. At high mass fractions, the filament remains quite thick (the final dimensionless radius at the midfilament is $h_f = 0.08$) and has poor axial uniformity. At lower mass fractions, the processability number P_0 decreases and the diameter of the filament can be reduced by several orders of magnitude ($h_f = 0.003$). The filament has much larger axial uniformity. In Fig. 10, we focus on the dynamics of the CABER experiment with $x_0 = 0.22$. Fig. 10(a) shows the shape of the liquid bridge going under capillary thinning and drying at times $t = 0$, $t = 5$ and $t = 10$. In Fig. 10(b) we plot the midfilament dimensionless radius $h_{mid}(t)$ as a function of dimensionless time. Keeping all the other simulation parameters equal, we also contrast this with the computation with no evaporative mass transfer ($P_0 = 0$), which shows a linear decrease of the radius at low strains because of the low initial value of the elasto-capillary number ($Ec_0 = 0.043$). At high strains, a transition to an elasto-capillary balance is observed and the radius of the filament decreases exponentially as predicted by theory [24]. In Fig. 10(c) we show the axial velocity profile at times $t = \{1, 4, 7, 10\}$. The mass

fraction of polymer at the midfilament is plotted in Fig. 10(d) as a function of time. At early times, we notice that the radius decreases almost linearly with time and the velocity profile shows capillary-driven drainage flow towards each quiescent region near the plates. However, at a dimensionless time $t \approx 4$ the solvent starts to evaporate at a faster rate and the dynamics of filament thinning are dramatically retarded (compared to the case $P_0 = 0$) because of increased viscoelasticity in the fluid. At time $t = 10$, the axial velocity profile is close to zero along the length of the filament, which means that drainage by convection stopped. However, the mass fraction of polymer keeps increasing even for $t \geq 10$ and the filament radius now decreases slowly, as a result solely of evaporation of the solvent.

5.3. Visco-capillary equilibrium and elasto-capillary equilibrium

The force balance during self-thinning of viscoelastic liquid bridges was investigated by Entov & Hinch [24] for $P_0 = 0$ (no evaporation) and $Ec_0 > 1$ using the FENE model. In Fig. 11(a), we show the evolution in time of the three terms appearing in the tensile force in Eq. (12): the solvent stress $3\beta_s \frac{\partial v}{\partial z}$, the capillary stress κ and the polymeric stress difference $T^p_{zz} - T^p_{rr}$. They are all evaluated at the midfilament ($z = \Lambda_0/2$). Because of the low value of the solvent viscosity compared to the solution viscosity ($\beta_s << 1$), we notice that the solvent stress does not enter the dominant balance at any time. This means that the parameter β_s does not play any physical role in the evolution of the filament profile; hence we can increase the value of β_s to improve numerical stability without affecting the dynamics of the filament evolution. At high mass fractions of polymer, the capillary stress and polymeric stress difference saturate and approach a plateau value. This means that a strong residual tensile stress remains in the fiber: the glass transition freezes the motion in the polymer network and the entangled polymer chains, stretched by the extensional flow, carry a residual tensile stress. In Fig. 11(c) and Fig. 11(d), we plot the absolute value of the various contributions at the midfilament of the axial and radial stress balances in Eq. (13) and Eq. (14). As $v = 0$ at $z = \Lambda_0/2$ (in the absence of inertia), the terms $v\frac{\partial T^p}{\partial z}$ are equal to zero at the midfilament and are not plotted. At early times, the axial stress (1) and the Newtonian term (5) form the dominant balance, and the other terms can be neglected. The filament is in visco-capillary equilibrium, which can be rationalized by the low initial value of the elasto-capillary number ($Ec_0 = 0.043$). At $t \approx 5$, the elastic terms (2) and (3) cross the

Newtonian term (5), which represents a transition from a visco-capillary balance to an elasto-capillary balance. For times $5 \leq t \leq 7$, the stresses grow approximately exponentially (Fig. 11(c,d)) and the mid point radius decreases approximately exponentially (Fig. 10(b)) as expected for a thinning filament in elasto-capillary equilibrium. At all times, the non-linear quadratic term (4), specific to the Giesekus equation can be neglected: this means that the system can also be well described by an Oldroyd-B fluid. However, retaining this term is essential at lower polymeric mass fractions to enable the model to describe break-up in finite time [39]. At very long times it is clear that the stresses saturate and the thinning process is arrested. In this region it becomes important to consider the role of solvent evaporation in more detail.

5.4. "Capillary arrest"

To obtain the overall continuity equation for the polymer solution, we sum up Eq. (1) and Eq. (8):

$$\frac{\partial h^2}{\partial t} + \frac{\partial (v h^2)}{\partial z} + 2hP_0(1-x) = 0 \tag{21}$$

In this equation, $\partial(vh^2)/\partial z$ represents the mass flux by axial capillary drainage towards the endplates, and $2P_0h(1-x)$ is the radial mass flux across the boundary from evaporation of the solvent. A comparison of the evolution of those two terms is shown in Fig. 11(b). Convection by capillary drainage is dominant up to $t = 7$ but its contribution to the total mass flux of solvent decreases as evaporation leads to an increase of the viscoelastic properties of the solution. After $t = 7$, the evaporation term is dominant and the radius of the thread at each axial location decreases primarily by pure solvent loss. We call this process "capillary arrest", when the first crossing point between convection and evaporation term is encountered. The second crossing point at $t \approx 12$ is not physical but depends highly on the compositional dependence close to the glass transition, which is not accurately accounted for in our model due to the paucity of data for $x \geq 0.35$.

5.5. "State space" for visco-elasto capillary thinning with drying

In order to understand the complex dynamics more completely, it is helpful to develop a framework for visualizing the different stages in the thinning and drying process. We define the instantaneous elasto-capillary number at time t $Ec_t = \lambda(t)\sigma/\eta_0(t)R_{mid}(t)$ evaluated at the midfilament, comparing the actual

visco-capillary time scale $t_{cap}(z = \Lambda_0/2) = \eta_0(t)R_{mid}(t)/\sigma$ and the actual relaxation time $\lambda(t)$. The transition from visco-capillary equilibrium to elasto-capillary equilibrium is thus expected to occur at $Ec_t = 1$. We also define the instantaneous processability number $P_t = \eta_0(t)\overline{h}_m/\sigma$ at time t comparing the actual visco-capillary time scale to the actual evaporation time scale $t_{evap}(z = \Lambda_0/2) = R_{mid}(t)/\overline{h}_m$. The transition from visco-capillary regime to "capillary arrest" is materialized by $P_t = 1$. For the transition from elasto-capillary equilibrium to "capillary arrest", we have to compare the actual evaporation time scale t_{evap} to the actual relaxation time λ. This transition happens when the product $Ec_tP_t = 1$.

Using instantaneous values of these dimensionless groups based on the output of the numerical simulation provides a useful tool to determine the balance of forces at time t. In Fig. 12, the output of the numerical simulation for a CABER experiment with $x_0 = 0.22$ is used to define a trajectory of the system in the "state space" defined by Ec_t-P_t. Each point is separated by a fixed dimensionless time step $\Delta t = 0.5$. The trajectory starts in the region of visco-capillary equilibrium, crosses the border $Ec_t = 1$ at $t = 5$, which is confirmed by Fig. 11(c) and crosses the "capillary arrest" border $P_t = 1$ at $t = 7$, in agreement with Fig. 11(b).

Drainage of fluid by capillary thinning is negligible for $P_t >> 1$; the viscosity is so large that axial transport is prevented and only evaporation is important. In Fig. 12, we notice that $P_t \approx 10^2$ at $t = 8$. At that time, we can read in Fig. 10(d) that $x_{mid} \approx 0.5$. We can conclude that convection by drainage can be neglected after $x = 0.5$, and that the exact correlations of viscosity and relaxation time close to glass transition do not have additional impact on the dynamics, which are driven solely by solvent loss. This justifies our simplification of using the extrapolation of the exponential laws determined experimentally for the viscoelastic properties of the polymer solution at moderate concentrations. We also notice that the trajectory through the "state space" approaches an asymptote as $P_t \to \infty$. This asymptote depends on the correlations chosen for the viscosity and relaxation time dependence on mass fraction. In the present compositional model, we have:

$$\frac{Ec_t}{Ec_0} = \frac{\lambda_0}{\lambda}\frac{\eta_0}{\eta_{00}}\frac{1}{h} = \frac{e^{-5(x-x_0)}}{h} \qquad \frac{P_t}{P_0} = \frac{\eta_0}{\eta_{00}} = e^{36(x-x_0)} \tag{22}$$

Eliminating the mass fraction from the second expression, we find:

$$\lim_{P_t \to \infty} Ec_t = \frac{1}{h_f} Ec_0 \left(\frac{P_t}{P_0} \right)^{-\frac{5}{36}} \tag{23}$$

where $h_f = R_f/R_0$ is the final equilibrium radius of the filament. Alternatively, if the shear modulus $G = \eta_0/\lambda$ is assumed independent of mass fraction, then Eq. 23 simplifies to the horizontal asymptote $\lim_{P_t \to \infty} Ec_t = Ec_0/h_f$.

5.6. Axial uniformity

In Fig. 13, we plot the axial curvature $\frac{h_{,zz}}{(1+h_{,z}^2)^{\frac{3}{2}}}$ at the midfilament, for a filament with $x_0 = 0.22$ modeled with a Giesekus model ($Ec_0 = 0.043$) or a Newtonian constitutive equation ($Ec_0 = 0$). We also report the axial uniformity for $x_0 = 0.24$ with a Giesekus model and for a Newtonian fluid with no drying ($P_0 = 0$, $Ec_0 = 0$). The degree of axial uniformity is controlled by two independent contributions: firstly strain hardening and secondly what we call "differential drying". The effect of strain hardening on uniformity of extensional flows was explained by Chang & Lodge [40], and is linked to axial variations of the extensional viscosity based on the degree of deformation or Hencky strain of a material element. A strong strain-hardening component requires $Ec_t > 1$ so that elasto-capillary equilibrium is reached before the fast drying process occurs. The $x_0 = 0.24$ has a lower axial uniformity because it starts from approximately the same initial value of Ec_0 but dries faster, thus it experiences a lower Hencky strain and smaller amount of strain hardening before solidifying. Moreover, there is a significant axial gradient of viscosity because fluid particles have different mass fractions along the fiber. The midfilament region dries faster because of the higher surface to volume ratio, and also has a higher viscosity than the neighboring fluid particles. We call this mechanism "differential drying". If we look at the Newtonian simulation for $x_0 = 0.22$, the fiber attains some level of uniformity by "differential drying". This axial uniformity is greatly enhanced by the strain hardening elastic response given by the Giesekus model.

5.7. Predicting the behavior of nanofibers

We used the macroscopic experiments performed with CABER to validate our model and determine the average mass transfer coefficient $\overline{h}_m$. We can now proceed to simulate the behavior of drying liquid filaments on the microscopic scale. We consider the "Brush-On" process on a micropatterned surface with 200×200 μm posts separated by $L_0 = 330$ μm. This means that $R_0 = 100$ μm and $\Lambda_0 = 3.3$. We

assume that the initial shape of the liquid bridge between two micropillars, resulting from the brushing motion, can be evaluated using the reversed squeeze flow. The simulation parameters are reported in Table 3. The evolution of the radius at the midfilament as a function of time is reported in Fig. 14. Because of the reduction in the plate radius, the initial value of the elasto-capillary number Ec_0 in the microfilament experiments is increased, while the value of P_0 remains constant as compared to CABER experiments. The numerical simulations show that this results in proportionally thicker fibers than the CABER experiments (Fig. 7) for the same initial mass fractions.

5.8. Designing polymer solutions for controlled radius reduction

We seek to exploit the useful tool of "state space" presented in Section 5.5 to "design" spinnable polymer solutions that enable user-selectable orders of magnitude reduction in the final filament radius. In order to achieve sufficient data density, numerical simulations in this section are implemented using a simpler $(0+1)$D (space+time) approximation (i.e. no axial curvature) of the form described in the paper by Entov & Hinch [24], coupled with our mass transfer model to account for solvent evaporation and the material parameters determined for the Giesekus model. Fig. 15 shows a map of the trajectories of the system in the "state space" of the $P_t - Ec_t$ diagram. Two different types of trajectories can be identified: when the initial processability number $P_0 < 10^{-2}$, the filament evolution starts with a vertical line corresponding to capillary thinning with almost no drying. The processability number remains small and constant in this regime. The importance of elastic effects grows as the radius decreases and the deformation rate steadily increases. When $Ec_t > 1$, elastic stresses begin to dominate the dynamics and the balance of forces in the thread cross over to elasto-capillary equilibrium. The radius of the thread still decreases until a sharp turning point occurs, corresponding to "capillary arrest" and a fast drying process. For $P_0 << 1$, it is clear from the figure that this turning point is independent of the initial elasto-capillary number Ec_0 for a given P_0. What does change is the time required to reach this point and the corresponding axial uniformity of the filament. By contrast, when the initial processability number $P_0 > 10^{-2}$, drying and capillary thinning occur simultaneously and at all times. This corresponds to small decreases in the total reduction in the radius and very low axial uniformity. The initial value of the processability number $P_0 = \overline{h}_m \eta_{00}/\sigma$ controls the amount of drainage possible by capillary thinning

before drying becomes dominant. In order to quantify those observations we have to determine when the turning point occurs in the $Ec_t - P_t$ "state space". This is the point at which a significant fraction of solvent has evaporated during the characteristic evolution time of the filament. This time scale can be the actual visco-capillary time scale t_{cap} or may be the fluid relaxation time λ depending on the force balance at time t. To develop an appropriate cross-over criterion, we can scale the dimensional version of the continuity equation for the polymer solution (Eq. 21) to reveal when the ratio of evaporative mass flux to the change in volume at the midfilament is equal an appropriately small value; here we select 1%. If the turning point happens during visco-capillary equilibrium, then we have at the turning point:

$$\frac{R\overline{h}_m}{\frac{\partial R^2}{\partial t}} \approx 10^{-2} \Leftrightarrow \frac{t_{cap} R\overline{h}_m}{R^2} \approx 10^{-2} \Leftrightarrow P_{(TP)} \approx 10^{-2} \tag{24}$$

where $t_{cap} = \eta_0 R/\sigma$ is the visco-capillary time scale based on the actual value of the variables and the subscript (TP) denotes turning point.

If the turning point happens during elasto-capillary equilibrium, this criterion translates into:

$$\frac{R\overline{h}_m}{\frac{\partial R^2}{\partial t}} \approx 10^{-2} \Leftrightarrow \frac{R\overline{h}_m \lambda}{R^2} \approx 10^{-2} \Leftrightarrow P_{(TP)} Ec_{(TP)} \approx 10^{-2} \tag{25}$$

The instantaneous processability number P_t remains almost constant at the initial value if $P_0 < 10^{-2}$, because the drainage by capillary thinning dominates the evaporative mass flux. However, the ratio of the mass flux of solvent compared to the mass flux from drainage increases (as shown in Fig. 11(b)), which will lead to a turning point. Eq. (25) then becomes $P_0 Ec_{(TP)} \approx 10^{-2}$. The elasto-capillary number at the turning point $Ec_{(TP)}$ can be related to the total radius reduction h_f by $h_f \approx R_{(TP)}/R_0 \approx \frac{Ec_0}{Ec_{(TP)}}$. Thus we can use these scalings to select the desired level of capillary thinning: if we want X orders of magnitude of radius reduction then $h_f = R_f/R_0 = 10^{-X}$ and Eq. (25) becomes:

$$P_0 Ec_0 \approx 10^{-2-X} \Leftrightarrow \frac{\lambda_0 \overline{h}_m}{R_0} \approx 10^{-2-X} \tag{26}$$

This analysis provides useful guidelines for rheological design of suitable polymer solutions for micro or nano fiber fabrication processes. First, the initial processability number must satisfy $P_0 < 10^{-2}$, otherwise, drainage by capillary thinning is prevented by significant evaporation, leading to thick fibers

and low axial uniformity. When $P_0 < 10^{-2}$ is satisfied, then we have the simple criterion $\frac{\lambda_0 \overline{h}_m}{R_0} \approx 10^{-2-X}$ to predict how many orders of magnitude X the polymeric fiber will thin before solidifying due to "capillary arrest". A remarkable result is that this criterion does not depend on the viscosity of the solution. The viscosity only determines how fast the processes of capillary thinning and drying occur. Another useful design tool is represented in Fig. 16, which maps the final equilibrium radius $h_f = R_f/R_0$ as a function of Ec_0 and P_0. At large values of each of those parameters, microfibers will be obtained. As Ec_0 and P_0 are decreased, radius reductions of two to three orders of magnitude can be obtained. The numerical criterion for break-up is arbitrarily chosen here at $h = 10^{-4}$. For the CABER experiments, this corresponds to $R_f = 0.3$ μm. It is found experimentally that the failure of the filament often happens on larger lengths scales. In these solidifying filaments, failure is not related to pinch-off at the middle of the filament but is often triggered by air perturbations breaking the thread at the point of connection to the quasi-static liquid droplet at the end-plate. For "Brush-On" type experiments with $R_0 = 100$ μm, a value of $h_f = 10^{-4}$ corresponds to a final radius $R_f = 10$ nm, which is a reasonable criterion for breakup. Axial uniformity of the fibers will be higher if high strains are achieved in the elasto-capillary region before the fast drying process (from Fig. 15, it is clear that this corresponds to $P_0 < 10^{-2}$ and $Ec_0 > 10^{-2}$).

6. Conclusion

We have developed a self-consistent, one-dimensional model describing the simultaneous capillary thinning and drying of viscoelastic threads. Rheological characterization showed that the dependence of the material functions on concentration can be really described by exponential laws over a wide range of concentrations. A simple binary mass transfer model allowed us to justify the choice of a constant mass transfer coefficient over the time scale of the experiment. The capillary thinning and drying problem can then be compactly represented using two dimensionless groups: the elasto-capillary number comparing visco-capillary thinning and elasticity in the fluid, and the processability number comparing the evaporation time scale to the visco-capillary time scale. As the thread undergoes capillary drainage calculations show that the balance of forces evolves, depending on the local concentration of the polymer and the rate of mass transfer across the surface. Analysis shows that the dynamics may involve either an

initial visco-capillary equilibrium or an elasto-capillary equilibrium, followed by a period of "capillary arrest", during which the axial convective motion (drainage induced by surface tension) is negligible compared to the process of solvent evaporation. The trajectory of the thinning thread and the final equilibrium radius can be mapped as a function of these two relevant dimensionless groups, providing useful rheological design for fabrication of micro and nano fibers.

The modeling and analysis presented in this paper can be applied to any free-surface process involving transient evolution in fluid viscosity and elasticity: for instance simultaneous polymerization and capillary thinning; or cooling, vitrefication and capillary thinning. Active stretching of the filament is also of interest to model new processes for "Direct-Write" fabrication of polymer fibers, investigated by Berry [41]. This can readily be included by modifying the velocity boundary conditions at the endplates. The present work can be extended with a two-dimensional analysis, accounting more accurately for concentration gradients and radial diffusion within the fluid. Additional improvements are also possible for the mass transfer model as well as coupling of evaporative cooling to the mass transfer. Although these additional complexities may change some of the quantitative features of the processes, the basic physics will still be governed by the "state space" shown in Fig. 15 and Fig. 16.

Acknowledgments

The authors would like to thank Prof. Bora Mikic for his help on the mass transfer modeling and Dr. Benjamin Seibold for several helpful discussions on numerical simulation. This investigation was funded by National Science Foundation NIRT Program (ECS-0506941). J.-C. Nave would like to acknowledge partial support by the National Science Foundation under grant DMS-0813648.

References

[1] M.R. Stan, P.D. Franzon, S.C. Goldstein, J.C. Lach, and M.M. Ziegler. Molecular electronics: from devices and interconnect to circuits and architecture. *Proceedings of the IEEE*, 91(11):1940–1957, 2003.

[2] X. Wang, C. Drew, S.H. Lee, K.J. Senecal, J. Kumar, and L.A. Samuelson. Electrospun nanofibrous membranes for highly sensitive optical sensors. *Nano Letters*, 2(11):1273–1275, 2002.

[3] L. Tong, R.R. Gattass, J.B. Ashcom, S. He, J. Lou, M. Shen, I. Maxwell, and E. Mazur. Subwavelength-diameter silica wires for low-loss optical wave guiding. *Nature*, 426(6968):816–819, 2003.

[4] Z. Huang, Y.Z. Zhang, M. Kotaki, and S. Ramakrishna. A review on polymer nanofibers by electrospinning and their applications in nanocomposites. *Composites Science and Technology*, 63(15):2223–2253, 2003.

[5] A. Ziabicki. *Fundamentals of Fibre Formation*. Wiley, New York, 1976.

[6] S.A. Harfenist, S.D. Cambron, E.W. Nelson, S.M. Berry, A.W. Isham, M.M. Crain, K.M. Walsh, R.S. Keynton, and R.W. Cohn. Direct drawing of suspended filamentary micro- and nanostructures from liquid polymers. *Nano Lett.*, 4(10):1931–1937, 2004.

[7] S.M. Berry, S.A. Harfenist, R.W. Cohn, and R.S. Keynton. Characterization of micromanipulator-controlled dry spinning of micro- and sub-microscale polymer fibers. *Journal of Micromechanics and Microengineering*, 16(9):1825–1832, 2006.

[8] A.S. Nain, C. Amon, and M. Sitti. Proximal probes based nanorobotic drawing of polymer micro/nanofibers. *Nanotechnology, IEEE Transactions on*, 5(5):499–510, 2006.

[9] A.S. Nain, J.C. Wong, C. Amon, and M. Sitti. Drawing suspended polymer micro-/nanofibers using glass micropipettes. *Applied Physics Letters*, 89(18):183105–3, 2006.

[10] A.V. Bazilevsky, V.M. Entov, and A.N. Rozhkov. Liquid filament microrheometer and some of its applications. *Third European Rheology Conference*, pages 41–43, 1990.

[11] A. Tripathi, P. Whittingstall, and G.H. McKinley. Using filament stretching rheometry to predict strand formation and "processability" in adhesives and other non-Newtonian fluids. *Rheologica Acta*, 39(4):321–337, 2000.

[12] Y. Ohzawa, Y. Nagano, and T. Matsuo. Studies on dry spinning. i. fundamental equations. *Journal of Applied Polymer Science*, 13(2):257–283, 1969.

[13] Z. Gou and A.J. McHugh. Two-dimensional modeling of dry spinning of polymer fibers. *Journal of Non-Newtonian Fluid Mechanics*, 118(2-3):121–136, 2004.

[14] W.W. Schultz and S.H. Davis. One-dimensional liquid fibers. *Journal of Rheology*, 26(4):331–345, 1982.

[15] D.T. Papageorgiou. On the breakup of viscous liquid threads. *Physics of Fluids*, 7(7):1529–1544, 1995.

[16] O.E. Yildirim and O.A. Basaran. Deformation and breakup of stretching bridges of Newtonian and shear-thinning liquids: comparison of one- and two-dimensional models. *Chemical Engineering Science*, 56(1):211–233, 2001.

[17] M. Yao, G.H. McKinley, and B. Debbaut. Extensional deformation, stress relaxation and necking failure of viscoelastic filaments. *Journal of Non-Newtonian Fluid Mechanics*, 79(2-3):469–501, 1998.

[18] J. Eggers and T.F. Dupont. Drop formation in a one-dimensional approximation of the navier-stokes equation. *University of Chicago*, 1992.

[19] M.G. Forest and Q. Wang. Change-of-type behavior in viscoelastic slender jet models. *Theoretical and Computational Fluid Dynamics*, 2(1):1–25, 1990.

[20] G.H. McKinley. Dimensionless groups for understanding free surface flows of complex fluids. *Soc. Rheol. Bull.*, 2005:6–9, 2005.

[21] W.K. Lewis and W.G. Whitman. The two-film theory of gas absorption. *Ind. Eng. Chem.*, 16:1215–1239, 1924.

[22] J. Eggers. Nonlinear dynamics and breakup of free-surface flows. *Reviews of Modern Physics*, 69(3):865–929, 1997.

[23] H. Giesekus. A simple constitutive equation for polymer fluids based on the concept of deformation-dependent tensorial mobility. *Journal of Non-Newtonian Fluid Mechanics*, 11(1-2):69–109, 1982.

[24] V.M. Entov and E.J. Hinch. Effect of a spectrum of relaxation times on the capillary thinning of a filament of elastic liquid. *Journal of Non-Newtonian Fluid Mechanics*, 72(1):31–53, 1997.

[25] S.H. Spiegelberg, D.C. Ables, and G.H. McKinley. The role of end-effects on measurements of extensional viscosity in filament stretching rheometers. *Journal of Non-Newtonian Fluid Mechanics*, 64(2-3):229–267, 1996.

[26] A. Bach, H.K. Rasmussen, and O. Hassager. Extensional viscosity for polymer melts measured in the filament stretching rheometer. *Journal of Rheology*, 47(2):429–441, 2003.

[27] H.L. Wagner and Herman L. The Mark–Houwink–Sakurada relation for poly(methyl methacrylate). *J. Phys and Chem. Ref. Data*, 16(2):165–173, 1987.

[28] W.W. Graessley. Polymer chain dimensions and the dependence of viscoelastic properties on concentration, molecular weight and solvent power. *Polymer*, 21:258–262, 1980.

[29] W.W. Graessley. *Polymeric liquids and networks: structure and properties*. Taylor and Francis, 2004.

[30] D.E. Bornside, C.W. Macosko, and L.E. Scriven. Spin coating of a PMMA/chlorobenzene solution. *Journal of The Electrochemical Society*, 138(1):317–320, 1991.

[31] R.B. Bird, Armstrong R.C., and Hassager O. *Dynamics of polymeric liquids, Second Edition*. Wiley-Interscience, New York, 1987.

[32] J. Crest. Formation of microfibers and nanofibers by capillary-driven thinning of drying viscoelastic filaments. Master's thesis, Massachusetts Institute of Technology, 2009.

[33] F.N. Kelley and F. Bueche. Viscosity and glass temperature relations for polymer-diluent systems. *Journal of Polymer Science*, 50(154):549–556, 1961.

[34] H. Fujita and A. Kishimoto. Diffusion-controlled stress relaxation in polymers. ii. stress relaxation in swollen polymers. *Journal of Polymer Science*, 28(118):547–567, 1958.

[35] J.D. Ferry and R.A. Stratton. The free volume interpretation of the dependence of viscosities and viscoelastic relaxation times on concentration, pressure, and tensile strain. *Colloid and Polymer Science*, 171(2):107–111, 1960.

[36] C.W. Shu and S. Osher. Efficient implementation of essentially non-oscillatory shock-capturing schemes. *J. Comput. Phys.*, 77(2):439–471, 1988.

[37] X.D. Liu, S. Osher, and T. Chan. Weighted essentially non-oscillatory schemes. *Journal of Computational Physics*, 115:200–212, 1994.

[38] Y.M. Stokes, E.O. Tuck, and L.W. Schwartz. Extensional fall of a very viscous fluid drop. *The Quarterly Journal of Mechanics and Applied Mathematics*, 53(4):565–582, 2000.

[39] M.A. Fontelos and J. Li. On the evolution and rupture of filaments in Giesekus and FENE models. *Journal of Non-Newtonian Fluid Mechanics*, 118(1):1–16, 2004.

[40] H. Chang and A.S. Lodge. A possible mechanism for stabilizing elongational flow in certain polymeric liquids at constant temperature and composition. *Rheologica Acta*, 10(3):448–449, 1971.

[41] S.M. Berry. *Characterization of a Direct-Write Method for Fabricating 3D Polymer Microfibers and Construction of Microscale Platforms.* PhD thesis, University of Louisville, 2009.

[42] C.A. Angell, J.M. Sare, and E.J. Sare. Glass transition temperatures for simple molecular liquids and their binary solutions. *The Journal of Physical Chemistry*, 82(24):2622–2629, 1978.

Physical properties of PMMA/chlorobenzene	Value
Glass transition temperature of PMMA (T_{g1}) (from Aldrich)	398°K
Glass transition temperature of chlorobenzene (T_{g2})[42]	128°K
Diffusion coefficient of PMMA	$7.24 \times 10^{-11} \times$
in chlorobenzene (D_{sl})[30]	$\exp\left(-\frac{0.240}{0.0277+(1-x)^{2.19}}\right)$ m^2/s
Diffusion coefficient of chlorobenzene in air (D_{sg}) at 25°C	7.3×10^{-6} m^2/s
Surface tension of concentrated solutions (σ)	0.04 N/m
Viscosity of chlorobenzene at 20°C (η_s)	0.8×10^{-3} Pa s
Atmospheric pressure (p)	1.013×10^5 Pa
Vapor pressure of chlorobenzene at 25°C (p_{s0}) (from MSDS)	1580 Pa
Mark-Houwink coefficients for PMMA	$a = 0.76$
and benzene at 30°C [27]	$K = 5.2 \times 10^{-6}$ m^3/kg

Table 1: Physical and rheological properties of PMMA and chlorobenzene solutions

$x_0(\%)$	$Ec_0 \times 10^{-2}$	$P_0 \times 10^{-3}$	$t_{cap0}(s)$
20	4.7	0.68	0.32
22	4.3	1.5	0.69
24	4.0	3.1	1.4
26	4.3	6.0	2.8
28	3.2	9.8	4.5

Table 2: Parameters of CABER numerical simulation for various mass fractions. $\alpha = 10^{-4}$, $\beta_s = 5 \times 10^{-2}$ (for numerical stability), $\Lambda_0 = 3.3$ are constant parameters over all concentrations.

$x_0(\%)$	Ec_0	$P_0 \times 10^{-3}$	$t_{cap0}(s)$
20	0.71	0.68	0.021
22	0.65	1.5	0.046
24	0.61	3.1	0.097
26	0.65	6.0	0.19
28	0.49	9.8	0.30

Table 3: Parameters for numerical simulation at a microscale geometry with $R_0 = 100$ μm and $L_0 = 330$ μm for various mass fractions. The Giesekus model parameters are held fixed at $\alpha = 10^{-4}$, $\beta_s = 5 \times 10^{-2}$ (for numerical stability) and the aspect ratio $\Lambda_0 = 3.3$ is constant over all concentrations.

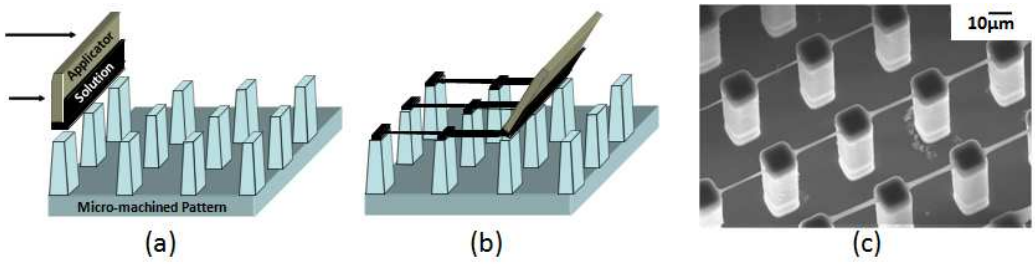

Figure 1: "Brush-On" process. (a) a polymer solution is spread on the edge of an applicator. (b) the applicator is moved horizontally at constant speed over a micropatterned surface, leaving a sheet of polymer solution that breaks into several liquid bridges between the top of two pillars. (c) after capillary thinning and drying, an array of aligned microfibers of average diameter 2 μm is obtained. SEM picture of fibers drawn on 10×10 μm pillars spaced by 20 μm with initial mass fraction $x_0 = 0.23$ PMMA ($\overline{\mathrm{M}}_\mathrm{w} = 996$ kg/mol) solution in chlorobenzene.

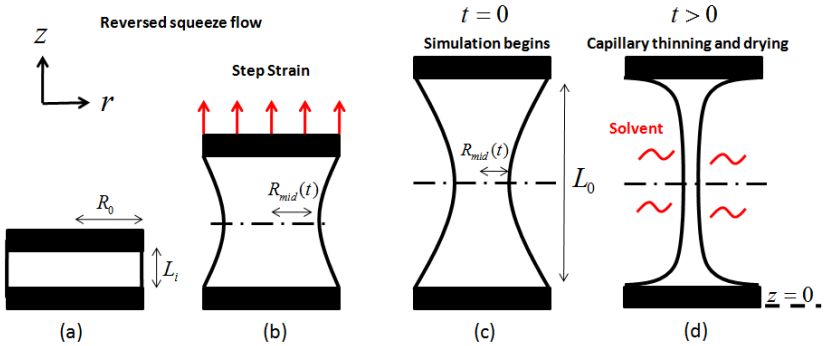

Figure 2: Definition of the geometry and coordinate system. (a) Initial configuration of the cylindrical filament. (b) Step strain modeled by a reversed squeeze flow. (c) Fixed length liquid bridge, numerical simulation begins. (d) Capillary thinning and drying between fixed plates leading to filament break-up or fiber formation.

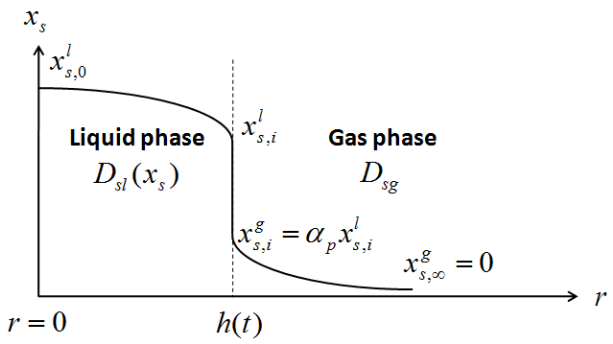

Figure 3: Schematic diagram of the diffusive mass transfer problem for an axial slice of the filament. Transient diffusion in the liquid phase has a driving force $x^l_{s,0} - x^l_{s,i}$, i.e. the difference between the solvent fraction in the liquid at the centerline and at the interface. Transient diffusion in the gas phase has a driving force $x^g_{s,i} - x^g_{s,\infty}$ corresponding to the difference between the solvent fraction in the gas at the centerline and far away from the filament. $D_{sl}(x_s)$ is the diffusion coefficient of solvent in liquid, D_{sg} the diffusion coefficient of solvent vapor in the gas phase and α_p is the partition coefficient of the gas/liquid interface.

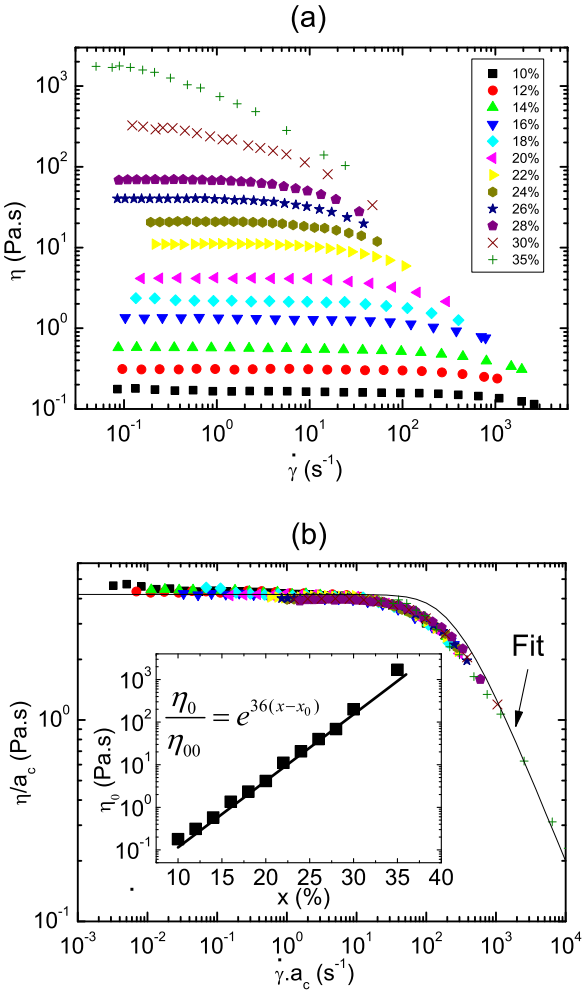

Figure 4: (a) Steady shear viscosity as a function of shear rate of PMMA ($\overline{\mathrm{M}}_{\mathrm{w}}$ = 996 kg/mol) in chlorobenzene for mass fractions ranging from $x_0 = 0.1$ to $x_0 = 0.35$. The data is collected at 23°C using cone and plate geometries from $x_0 = 0.18$ to $x_0 = 0.35$ and a double gap Couette geometry at lower concentrations. (b) Master curve using time-concentration superposition with a reference at $x_0 = 0.2$. The shift factor $a_c = \eta_0/\eta_{00}$ is the same for horizontal and vertical shifting. The inset shows the zero shear rate viscosity as a function of mass fraction, which is fitted to an exponential law. The black line is the steady shear flow Giesekus material function with $\alpha = 10^{-4}$.

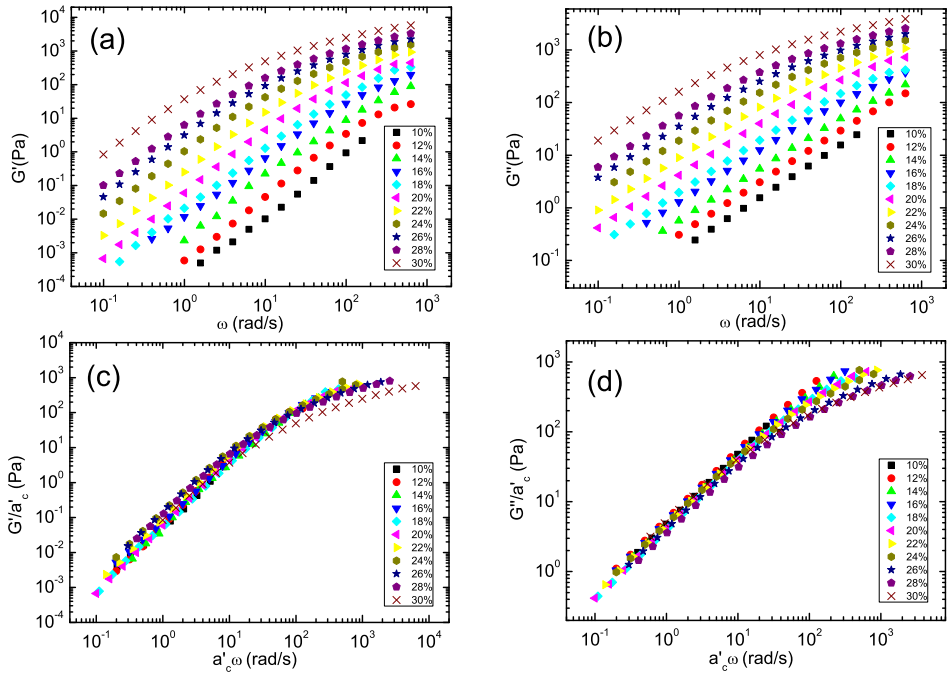

Figure 5: Small amplitude oscillatory shear as a function of frequency of PMMA ($\overline{\mathrm{M}}_{\mathrm{w}} = 996$ kg/mol) in chlorobenzene for mass fractions ranging from $x_0 = 0.1$ to $x_0 = 0.3$. The data is collected at 23°C. (a) and (b) correspond respectively to G' and G''. The data is collapsed on a master curve in (c) and (d) using time-concentration superposition with a reference at $x_0 = 0.2$. The shift factor a'_c is the same for both horizontal and vertical shifting in both G' and G''.

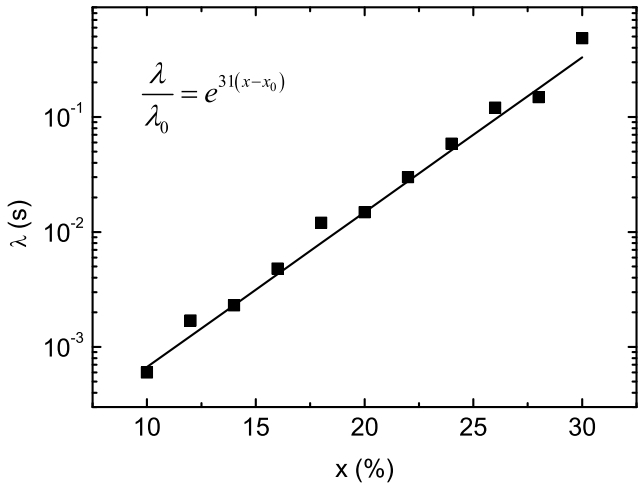

Figure 6: Average relaxation time as a function of mass fraction for PMMA ($\overline{\mathrm{M}}_{\mathrm{w}} = 996$ kg/mol) in chlorobenzene. The data is fitted to an exponential law, represented by the black line.

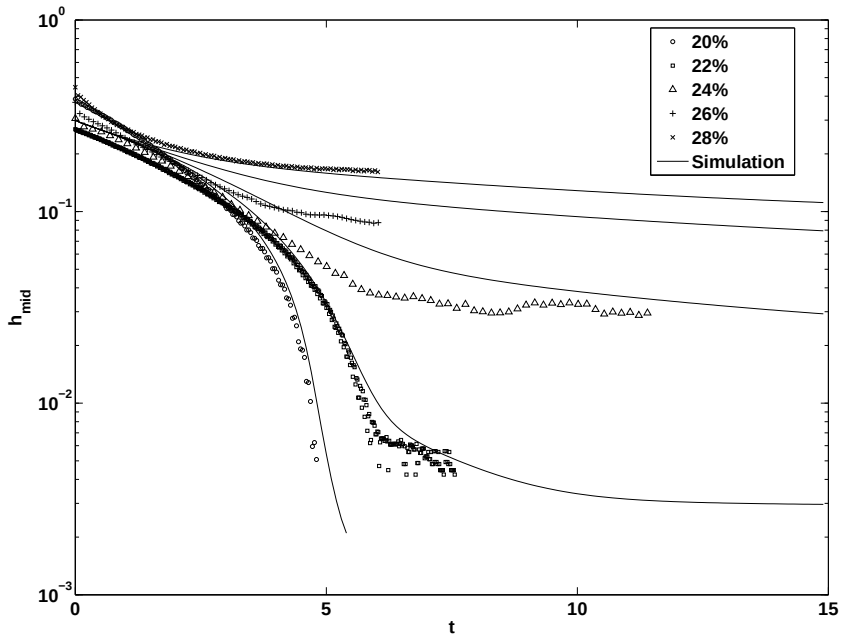

Figure 7: Dimensionless radius at the midfilament as a function of dimensionless time for initial mass fractions between $0.2 \leq x_0 \leq 0.28$. The symbols correspond to CABER experimental data and the continuous lines to numerical simulation. Parameters for numerical simulation are reported in Table 2. The experimental data for $x_0 = 0.26$ and $x_0 = 0.28$ is truncated because of gravitational sagging. At $x_0 = 0.2$ and $x_0 = 0.22$, air perturbation rapidly breaks the junction between the thin fiber and the polymer droplet.

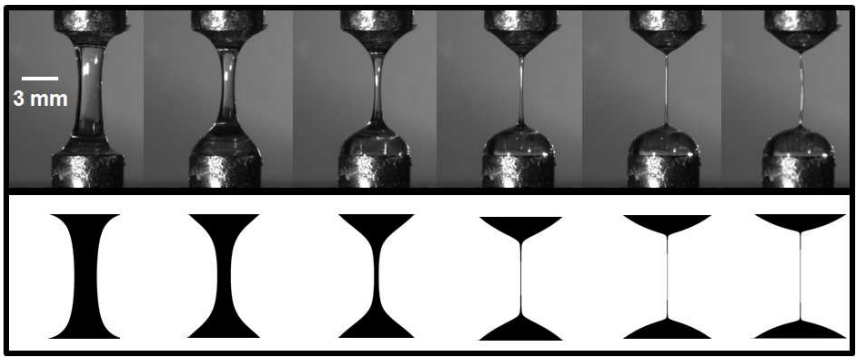

Figure 8: Comparison of the shape of the filament between CABER experiment and numerical simulation for $x_0 = 24\%$, $Ec_0 = 0.040$, $P_0 = 3.1 \times 10^{-3}$. The images are separated by a constant dimensionless time interval $\Delta t = 2$.

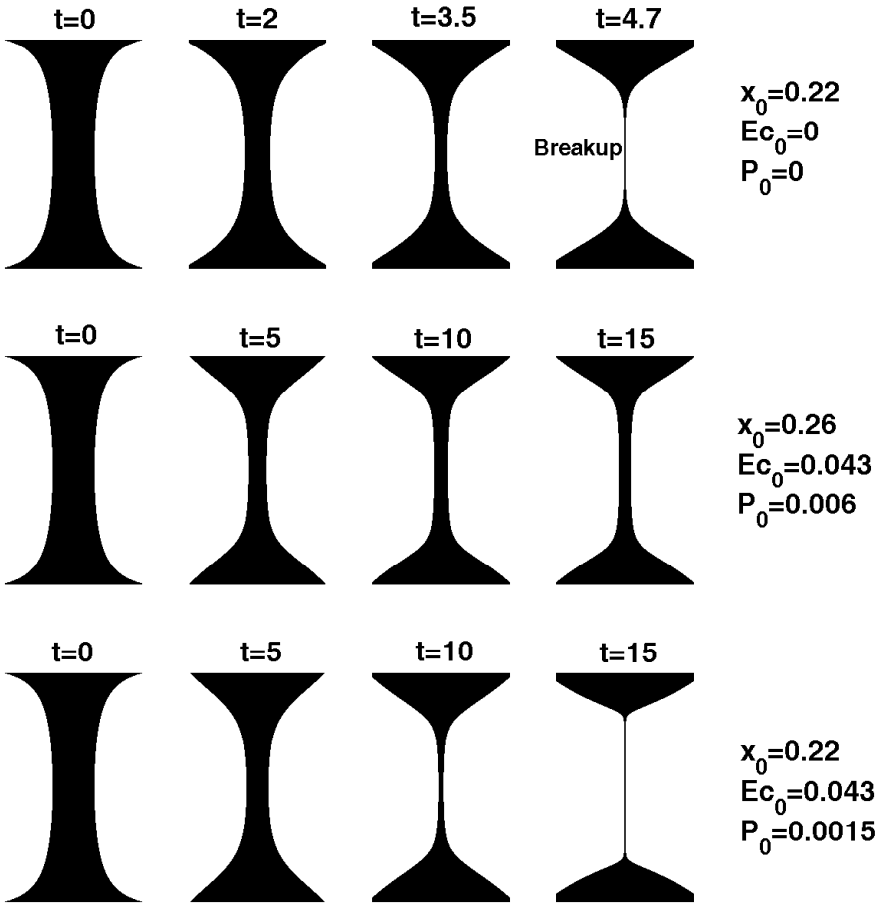

Figure 9: Comparison of the shape of the filament for a viscous Newtonian fluid $Ec_0 = 0$ with no drying $P_0 = 0$(top), for a PMMA/chlorobenzene solution with initial mass fractions $x_0 = 0.26$ (middle) and $x_0 = 0.22$ (bottom). The solvent viscosity ratio is $\beta_s = 0.05$ and the aspect ratio $\Lambda_0 = 3.3$ in all simulations. Time is scaled with the visco-capillary timescale $t_{cap0} = \eta_{00} R_0/\sigma$.

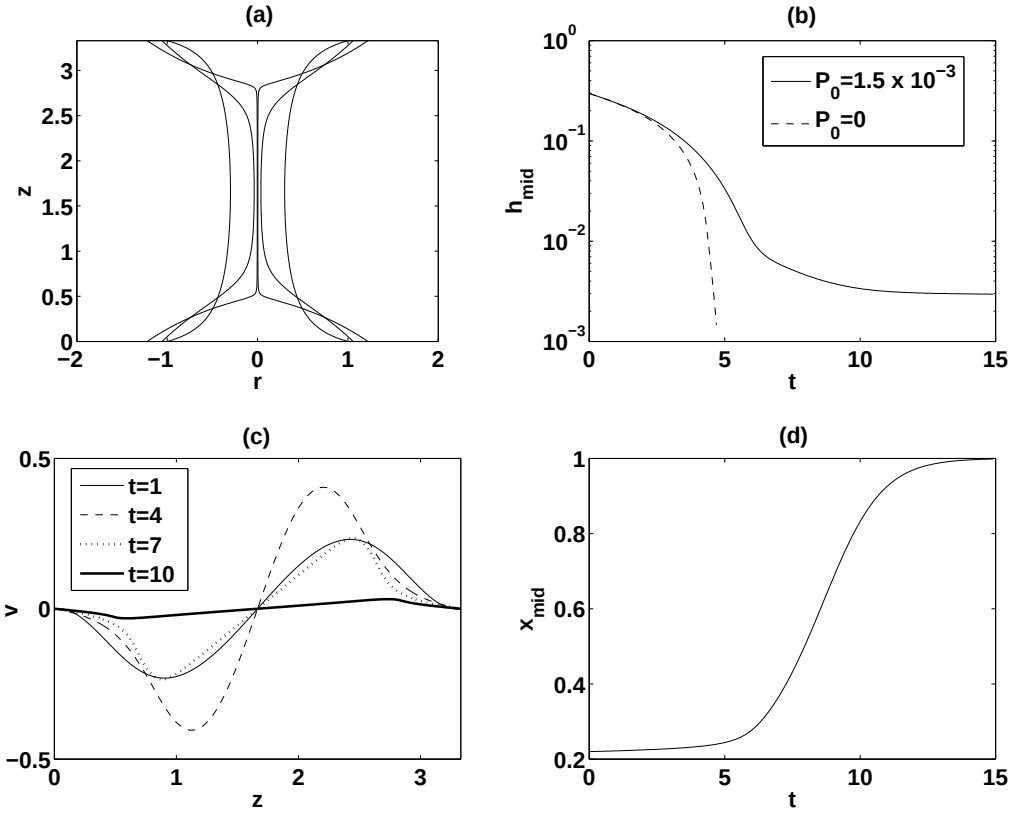

Figure 10: Simulation of the CABER experiment for $x_0 = 0.22$, $Ec_0 = 0.043$, $P_0 = 1.5 \times 10^{-3}$. (a) Shape of the filament at $t = 0$, $t = 5$, $t = 10$. (b) Evolution of the radius at the midfilament with time. (−): simulation with evaporation, (- -): simulation with no evaporation ($P_0 = 0$, $Ec_0 = 0.043$). (c) Velocity profile at $t = 1, 4, 7, 10$. (d) Mass fraction of polymer at the midfilament as a function of dimensionless time.

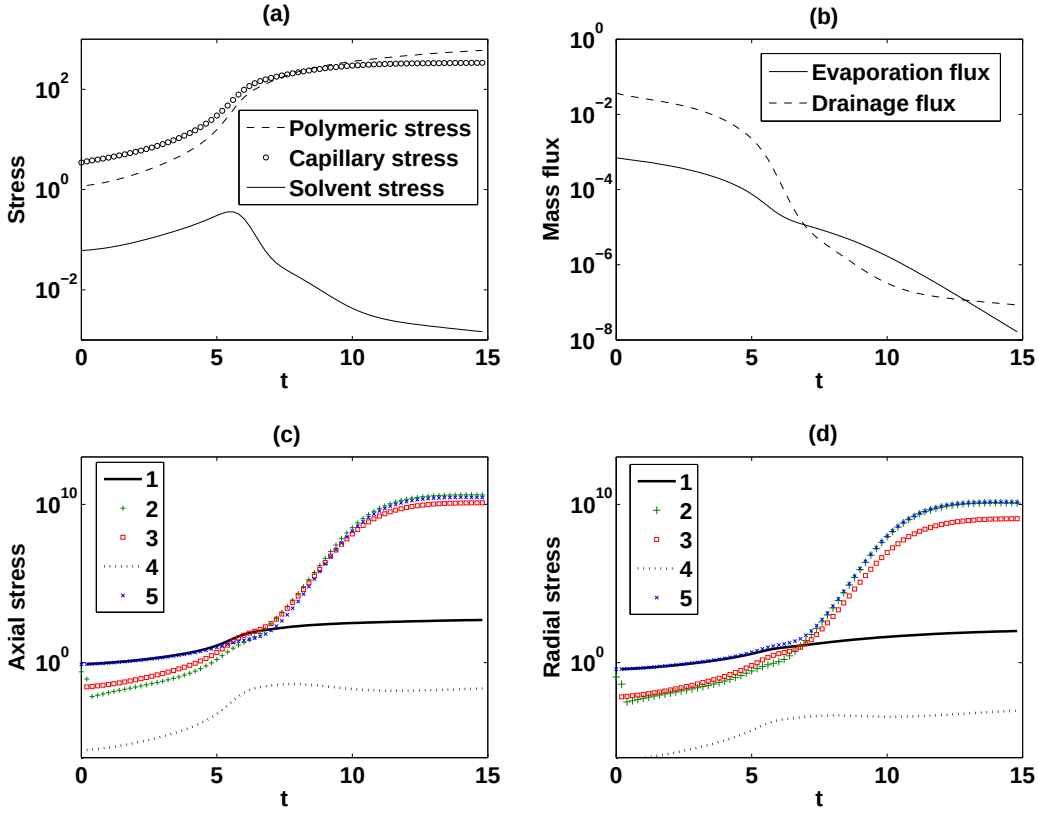

Figure 11: Stress and mass flux evolution at the midfilament for a CABER experiment with $x_0 = 0.22$ (a) Contribution of the three components of the tensile stress in Eq. (12) as a function of time. (b) Evolution of the drainage mass flux $\frac{\partial(vh^2)}{\partial z}$ along the filament and the evaporative mass flux $2P_0h(1-x)$ across the boundary in Eq. (21). (c) Axial stress terms in Eq. (13): (1) T^p_{zz}; (2) $Ec_0\frac{\lambda(x)}{\lambda_0}\frac{\partial T^p_{zz}}{\partial t}$; (3) $Ec_0\frac{\lambda(x)}{\lambda_0}2\frac{\partial v}{\partial z}T^p_{zz}$; (4) $\frac{\lambda(x)}{\lambda_0}\frac{\eta_{p0}(x_0)}{\eta_p(x)}\beta^{-1}\alpha Ec_0(T^p_{zz})^2$; (5) $2\beta\frac{\eta_p(x)}{\eta_{p0}(x_0)}\frac{\partial v}{\partial z}$. (d) Absolute value of the radial stress terms in Eq. (14): (1) $\left|T^p_{rr}\right|$; (2) $\left|Ec_0\frac{\lambda(x)}{\lambda_0}\frac{\partial T^p_{rr}}{\partial t}\right|$; (3) $\left|Ec_0\frac{\lambda(x)}{\lambda_0}\frac{\partial v}{\partial z}T^p_{rr}\right|$; (4) $\frac{\lambda(x)}{\lambda_0}\frac{\eta_{p0}(x_0)}{\eta_p(x)}\beta^{-1}\alpha Ec_0(T^p_{rr})^2$; (5) $\left|-\beta\frac{\eta_p(x)}{\eta_{p0}(x_0)}\frac{\partial v}{\partial z}\right|$.

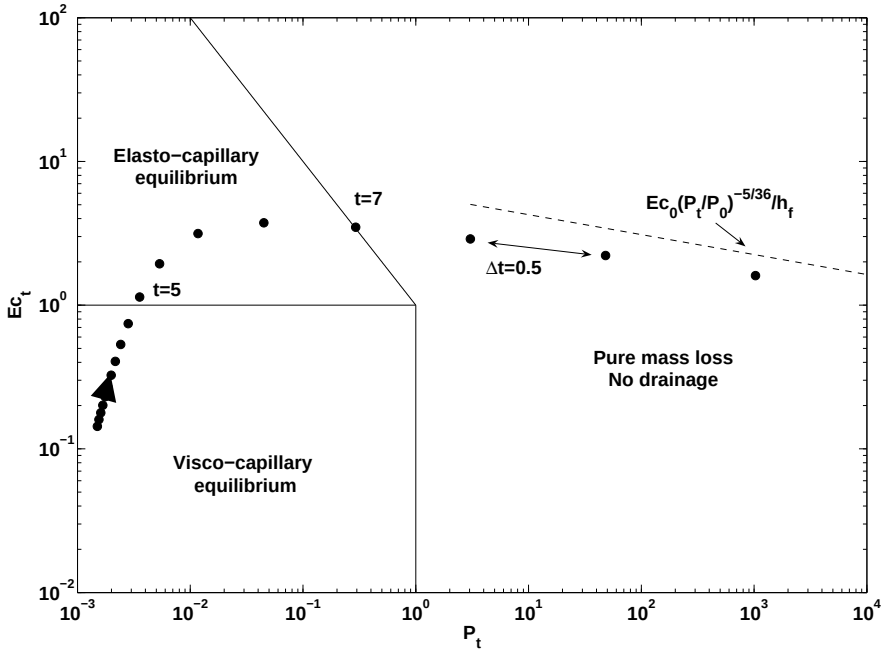

Figure 12: "State space" for $x_0 = 0.22$, $Ec_0 = 0.043$, $P_0 = 0.0015$. Ec_t is the instantaneous elasto-capillary number at the midfilament, P_t is the instantaneous processability number at the midfilament. The black dots materialize the trajectory computed by numerical simulation at fixed time intervals of $\Delta t = 0.5$.

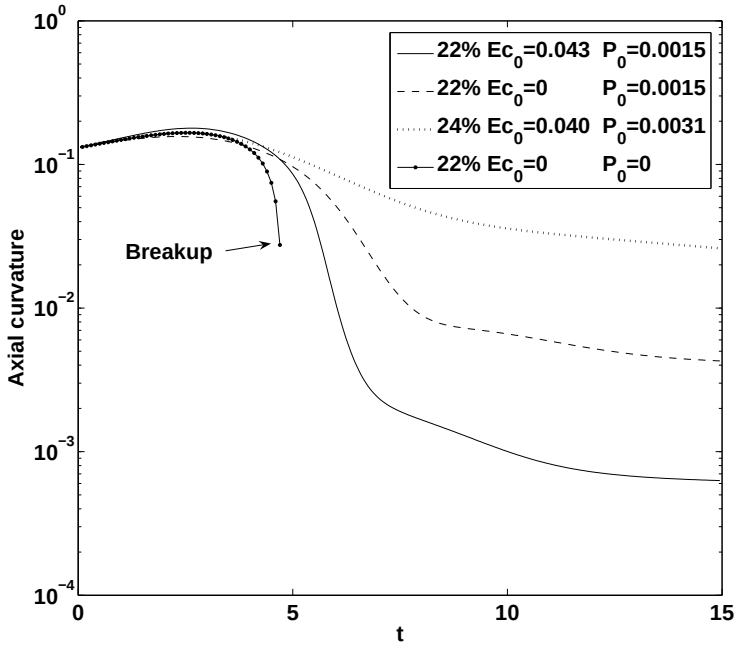

Figure 13: Comparison of the axial curvature $h_{,zz}/(1+h_{,z}^2)^{\frac{3}{2}}$ evaluated at the midfilament as a function of dimensionless time for Giesekus or Newtonian fluids with various processabilities. Axial uniformity has a differential drying component ($x_0 = 0.22$, $Ec_0 = 0.043$, $P_0 = 0$, shown by the dashed line) and a strain hardening component, which is the extra gain of uniformity for viscoelastic fluids ($x_0 = 0.22$, $Ec_0 = 0.043$, $P_0 = 0.0015$).

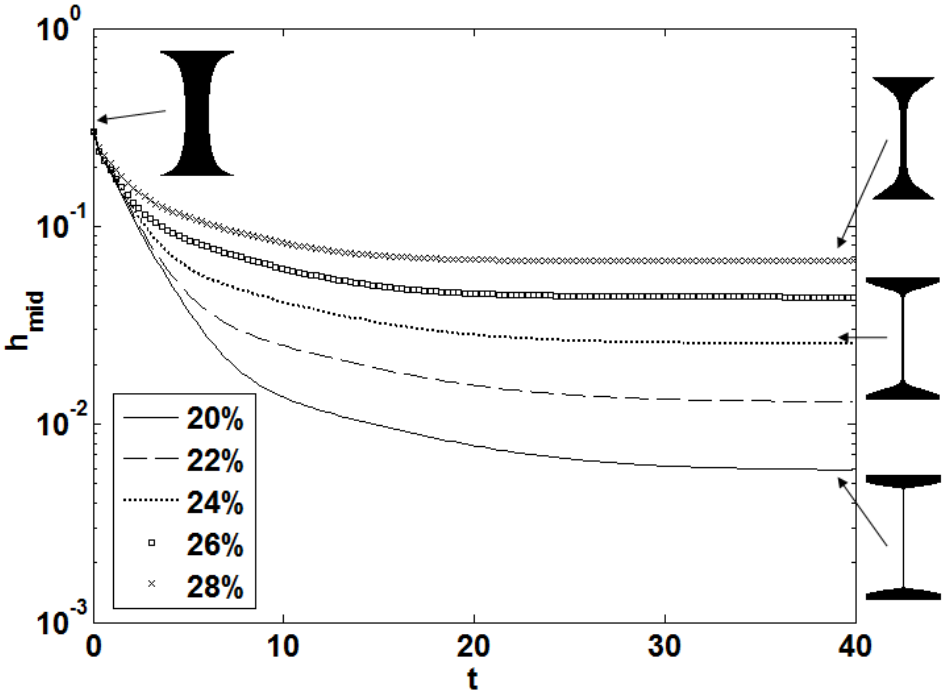

Figure 14: Prediction of thinning dynamics for a geometry with initial conditions $R_0 = 100$ μm, $L_0 = 330$ μm. The relevant values of the parameters for numerical simulation are reported in Table 3.

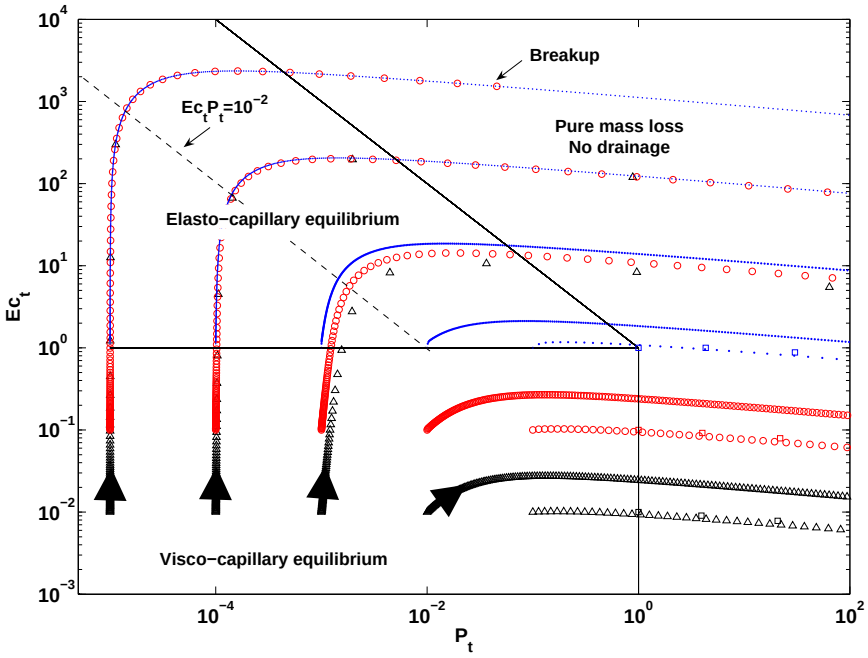

Figure 15: "State space", mapping the trajectories in the $Ec_t - P_t$ plane, with $10^{-2} < Ec_0 < 1$ and $10^{-5} < P_0 < 1$. For computational convenience, the simulations are run with a $(0+1)$D (space+time) model neglecting axial curvature.

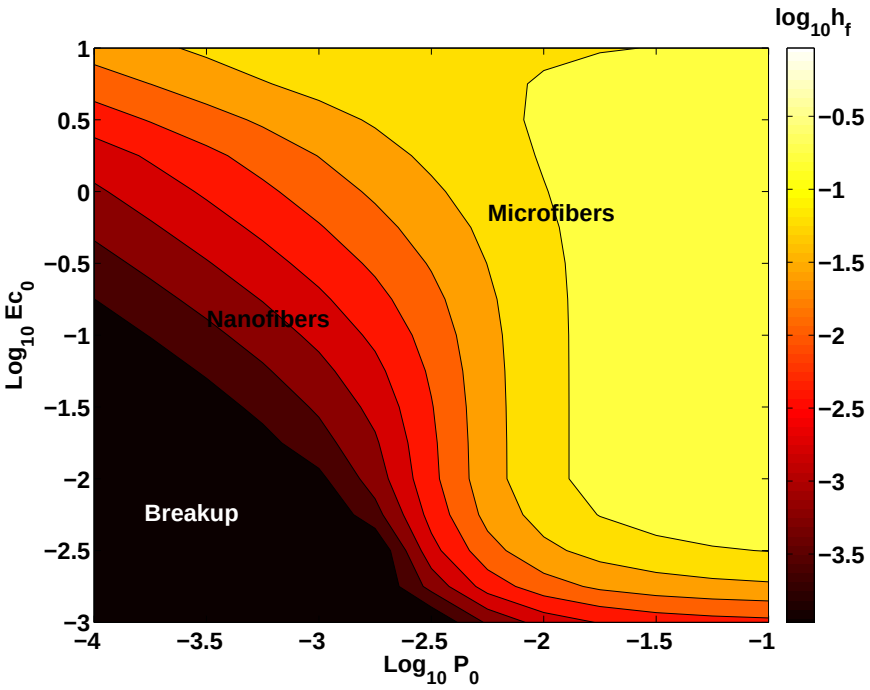

Figure 16: Map of the equilibrium radius as a function of Ec_0 and P_0 with $x_0 = 0.22$. The shading represents the radius reduction on a logarithmic scale, $\log_{10}(h_f)$. The simulations are run with a $(0+1)$D (space+time) model neglecting axial curvature, and assuming a constant mass transfer coefficient. Simulations are stopped at $h = 10^{-4}$ (corresponding to fibers below 10 nm assuming $R_0 = 100$ μm), which is considered as a numerical criterion for breakup of the fiber, or failure of the continuum description of the material properties.